Hybrid compactive faults formed during burial in micritic limestone (Montpellier area, France)

Grégory Ballas, Flavia Girard, Yannick Caniven, Roger Soliva, Bernard Célérier, Romain Hemelsdaël, Sylvain Mayolle, Aurélien Gay, Michel Séranne

Hybrid compactive faults formed during burial in micritic limestone (Montpellier area, France)

GRÉGORY BALLAS[1*], FLAVIA GIRARD[1], YANNICK CANIVEN[1], ROGER SOLIVA[1], BERNARD CÉLÉRIER[1], ROMAIN HEMELSDAËL[1], SYLVAIN MAYOLLE[1], AURÉLIEN GAY[1], MICHEL SÉRANNE[1]

1 Géosciences Montpellier, Université de Montpellier, CNRS, France.

**Correspondence: gregory.ballas@umontpellier.fr*

ABSTRACT: Detailed fieldwork, analyses including SEM and EBSD investigations, and dynamic inversion method are used to describe and propose a conceptual model for the formation of compactive faults related to burial in micritic lacustrine-palustrine limestones (Eocene, Pyrenean foreland basin, South of France). These faults are characterized by sinuous shape, no calcite precipitation and no macroscopic fault core evidencing their development in poorly consolidated sediments. The fault pattern is composed of two sub-synchronous systems of conjugate meter-scale faults (a normal-sense system and a strike-slip system), each one with high dihedral angle (130°) and sometimes showing continuity between faults of both sets. Their pervasive distribution, angle relative to the maximum principal stress direction, incipient shear-offset, porosity reduction, their crystallographic preferred orientation, and the "ridge and groove" morphology of their slickenside, all argue for a hybrid compactive and shear deformation process combining disaggregation, comminution, and pressure-solution-recrystallization processes. A conceptual model using estimated stress path and theoretical yield envelope is proposed to explain their formation along the end cap part during early burial and compaction of the

limestone beds. The slope to the South associated to the syn-sedimentary basin flexure is proposed to trigger their specific pattern.

.

Key-words: compactive faults, shear localization, pressure-solution, crystallographic preferred orientation, micritic limestone

1. Introduction

In micritic carbonate rocks, it is generally considered that fault initiate by a combination of various deformation structures such as veins, shearing planes, and/or compactive pressure-solution seams (Peacock and Sanderson, 1995; Willemse et al., 1997; Mazzoli and Di Bucci, 2003; Crider and Peacock, 2004; Micarelli and Benedicto, 2008; Delle Piane et al., 2017 and references therein). Faults mainly grow by propagation and segment linkage (Kelly et al., 1998; Ferrill and Morris, 2003; Soliva and Benedicto, 2004; Agosta et al., 2012; Roche et al., 2012; Ferrill et al., 2017; Mayolle et al., 2019 among others). Because fine-grained carbonates are generally of low-porosity, fracturing and brecciation are dominant in fault zones, expressing dilation and shear behaviour (Micarelli et al., 2006; Bussolotto et al., 2015; Balsamo et al., 2016). This deformation can progressively evolve into cataclastic processes within the main deformation area called the “fault core” (Billi, 2005; Hausegger et al., 2010; Schröckenfuchs et al., 2015; Ferraro et al., 2018). It can be accompanied by other various processes generally related to seismic events, i.e. clast-cortex grains, calcite crystallographic preferred orientation (CPO), or fluidized layers (Delle Piane et al., 2017; Demurtas et al., 2019). In such model, compactional processes are generally restricted to specific areas, such as fault dip changes (Ferrill et al., 2020)

45 or fault tips (Rispoli, 1981; Petit and Mattauer, 1995; Agosta et al., 2010). Compaction by
46 pervasive pressure-solution can also occur within the cataclastic zone, showing scaly foliation
47 (Bullock et al., 2014; Clemenzi et al., 2014). However, fault initiation by compaction processes
48 (mainly pressure-solution pressure-solution but also disaggregation and cataclasis) remains
49 unclear, especially in micritic carbonates (Billi, 2003; Graham et al., 2003; Agosta and Aydin,
50 2006).

51 Conversely, fault initiation by shear and compaction failures is well known in porous and
52 granular rocks such as sandstones (Antonellini and Aydin, 1994; Ballas et al., 2014; Fossen et al.,
53 2018), grainstones (Tondi et al., 2006; Cilona et al., 2012; Antonellini et al., 2014; Rotevatn et
54 al., 2016) or chalks (Wennberg et al., 2013; Kaminskaite et al., 2019). In such lithologies, faults
55 initiate by deformation bands showing different micro-mechanisms (Fisher and Knipe, 2001;
56 Aydin, 2006; Fossen et al., 2007) and various ratios of shear to compaction; i.e. pure compaction
57 bands (Mollema and Antonellini, 1996; Agosta et al., 2010; Rotevatn et al., 2016), shear-
58 enhanced compaction bands (Eichhubl et al., 2010; Ballas et al., 2013; Fossen et al., 2015),
59 compactive-shear bands (Saillet and Wibberley, 2013), and shear bands (Rotevatn et al., 2008).
60 Cataclastic processes are dominant and the related grain crushing induces pore collapse and
61 porosity reduction (Antonellini and Aydin, 1995; Fossen and Bale, 2007; Ballas et al., 2015)
62 leading to material hardening and shear localization (Aydin and Johnson, 1978; Schultz and
63 Fossen, 2002; Shipton and Cowie, 2003; Philit et al., 2018). Other micro-mechanisms; such as
64 disaggregation (grain rotation, torsion or displacement), or pressure-solution-recrystallization; are
65 described in deformation bands and faults (Cilona et al., 2012; Ballas et al., 2013; Philit et al.,
66 2015; Tavani et al., 2018a; Kaminskaite et al., 2019 among others). However, these processes
67 remain difficult to integrate in mechanical model such as the one developed for cataclastic

68 structures (Saillet and Wibberley, 2010; Soliva et al., 2013, 2016; Robert et al., 2018; Fossen et
69 al., 2018) because of the lack of combined descriptive-mechanical approach on such deformation
70 features.

71 Mechanical concepts suggest a potential formation of compactive-shear structures under
72 progressive burial, i.e. out of regional tectonic influence (Soliva et al., 2013). However, only few
73 natural examples propose compactive shear localization under gravitational loading (Guiraud and
74 Séguret, 1987; Wennberg et al., 2013), whereas almost all described compactive-shear structures
75 are related to tectonic stresses. During progressive burial, compaction follows general porosity
76 reduction curves (Ehrenberg and Nadeau, 2005) but can also localize bed parallel structures, such
77 as compaction bands (Aydin and Ahmadov, 2009; Rustichelli et al., 2012) or stylolites (Laronne
78 Ben-Itzhak et al., 2014). The part of these localization structures within the whole compaction of
79 sediment remains unclear. A better understanding of compactive-shear structures initiation
80 appears necessary, especially within fine-grained materials and under burial "gravitational"
81 loading.

82 In such context, we investigate a network of meter-scale compactive-shear structures exposed
83 within micritic continental limestone in the Aumelas - Hérault basin in the South of France
84 (Montpellier area). Detailed fieldwork, natural light, SEM and EBSD (scanning electron
85 microscopy, electron backscatter diffraction) microstructural investigations, and kinematic
86 inversion method have been used to describe the fault systems and discuss the mechanisms and
87 triggers. Theoretical mechanical models are used to discuss the origin of such structures.

88 **2. Methods**

89 *2.1. Field observations and measurements*

90 Sedimentological log of the main studied section was done to identify the relationship between
91 the occurrence of fault and bed characteristics. Beds are analyzed following the Dunham
92 classification (*M*: Mudstone, *W*: Wackstone, *P*: Packestone, *G*: Grainstone, *B*: Boundstone + *C* to
93 identify clays). Evidences of subaerial alterations (desiccation, karstification, brecciation)
94 observed on bed surfaces and the beds affected by fault sets (i.e. the location of fault networks in
95 the sedimentary succession) are also reported.
96 The geometry of the fault network is analyzed from stereographic data collected using compass
97 and digit tablet (FieldMOVE software). These data are reported on stereoplots and histograms of
98 dip and rake, i.e. the angle between the slickenline and the strike direction of individual fault
99 planes. The data are presented after restoring the bedding to horizontal.
100
101 *2.2. Microstructure and rock properties*

102 Nine polished thin-sections were cut from blocks sampled below fault slickensides previously
103 impregnated by epoxy resin. These thin-sections were cut in the dip-slip direction of faults (6
104 thin-sections) or the strike direction of faults (3 thin-sections) to analyze fault micro-mechanisms
105 and kinematic criteria (evidence and sense of shear). They were analyzed by backscattered
106 electron imagery using a FEI Quanta 200 environmental scanning-electron microscope (SEM).
107 Mosaics of SEM backscattered electron images, with a gray-scale intensity range from 0 to 255,
108 were obtained and used to observe deformation features and to estimate the porosity of the
109 deformed zones and the host rocks (2D porosity obtained from black areas on SEM images).
110 Several SEM images were also acquired on 3D blocks to observe grains and slickensides micro-
111 morphology. Analyses with optical microscope in natural or cross-polarized light, and
112 cathodoluminescence mode were also used to identify potentially different cement phases.

Electron BackScatter Diffraction (EBSD) analyses were done in the host rocks and along the fault zones, including steps and fault core. This analysis edits a map of the particles form their crystallographic assemblage and allows analyzing their size, shape and crystallographic orientation. Data were collected with the scanning electron microscope CamScan Crystal Probe X500FE and were processed using AZtecHKL software (Oxford Instruments). The acquisition was done with a 0.3-0.4 μm step size at a working distance of 25 mm. Grains were reconstructed from orientation data and their boundaries were defined as having a misorientation angle between neighboring pixels of > 5°. The grain slope (i.e. the angle of the grain longer axis with respect to vertical) was measured on grains showing surface area larger than 5 μm in order to avoid artefact due to the image resolution. These data are represented on rose diagram. Crystallographic orientations are represented on stereographic diagram (equal area, lower hemisphere) and the multiple of the uniform distribution (*m.u.d.* value) is used to estimate the crystallographic preferred orientation of grains (CPO). Calcite twinning is automatically mapped using the AZtecHKL software.

2.3. Fault slip and stress analysis

The state of stress during fault slip is obtained by inversion of the fault and slickenline data (Angelier, 1984) with the FSA software that was developed to analyse various aspects of the relationship between fault slips and stresses (Tajima and Célérier, 1989; Burg et al., 2005; Célérier, 2020). The inversion seeks the stress tensor that best align shear stress with observed slickenlines (Wallace, 1951; Bott, 1959) and uses the random search proposed by Etchecopar et al. (1981). This method allows to invert either the whole dataset in the case of monophase data or only a fraction of the dataset in the case of polyphase data. It yields the principal stress

orientations s_1, s_2, s_3, and stress tensor aspect ratio $r_0 = (\sigma_1-\sigma_2) / (\sigma_1-\sigma_3)$, where $\sigma_1 \geq \sigma_2 \geq \sigma_3$ are the principal stress magnitudes corresponding to the orientations s_1, s_2, s_3. We use the quality criterion proposed by Heuberger *et al.* (2010) to distinguish robust solutions from statistical artifacts. It is based on a comparison between the total number of data (N_{total}), the number of data with a rake misfit lower than 15° (N_{exp15}), and the number of data ($N0_{exp15}$) that could be obtained below the same misfit by inverting a random dataset of the same size N_{total}. The result of this comparison is summarized by an integer quality index, *InvQual*, which varies from -1 for barely acceptable solutions to 2 for robust estimates.

3. Geological Setting

3.1. Regional tectonic framework

The Aumelas - Hérault basin is located 20 km to the west of Montpellier city in the South of France (Fig. 1a). This basin form a part of the continental foreland basin developed at the front of the Montpellier thrust (also called North Pyrenean Frontal Thrust) (Arthaud & Séguret 1981). This thrust is related to the Pyrenean orogeny occurring in this area during two main shortening events, during Early Paleocene and Late Eocene. A relatively quiescent phase of tectonic activity occurred during Lower Eocene (Debrand-Passard et al., 1984) when carbonate lacustrine-palustrine sequence were deposits (Bonnet *et al.,* 1971). However, the accommodation of a 300-500 m thick sedimentary sequence showing locally growth strata (synsedimentary folding) in lacustrine deposits, indicates that some moderate tectonic activity remained during this period.

The studied outcrops are located along the A750 highway, at the “La Taillade” site (Lat. 43°37'36N; Long. 3°35'54"E, Fig. 1a). This area is located in front of the WNW-ESE St Bauzille

158 Thrust (reactivated Mesozoic normal-fault) and close to the change from NE-SW to EW trend of
159 the main Montpellier Thrust. Lacustrine-palustrine limestones were mainly folded and faulted
160 during Late Eocene second shortening phase of the Pyrenean orogeny (Fig. 1b). These strata are
161 now tilted 15-30° to the S and SW (up to 65° in the central part of the section, Fig. 2a), according
162 to their location in the fore-bulge of the Pyrenean thrusts and to the tilting of the NE-trending
163 Hérault half-graben during Oligocene rifting (Maerten & Seranne 1995). We note that the
164 maximum burial reached by the studied section is difficult to evaluate due to an uplift (>100 m)
165 and erosion during late Miocene (Séranne et al., 2002). However, we consider a maximum burial
166 in an order of magnitude of 100 m since Oligocene sediments are not deposited above the study
167 site (only formed in half-grabens) and the studied limestone section corresponds to the upper part
168 of the Eocene sequence.

169

170 *3.2. Host rock characteristics*

171 The main outcrop lies at the top of the 300 m thick "Lutetian" limestones strata related to a
172 lacustrine-palustrine system (Hartenberger et al., 1969) (Fig. 2). The studied section is limestone
173 dominated and shows a succession of mostly 25-50 cm thick, stacked, tabular carbonate beds
174 (Figs. 2 b, c). The beds are mainly composed of a massive white mudstone including whole or
175 fragments of fossils of continental gastropods (*limnea* and *planorbis*) and ostracods bioclasts. We
176 note the presence of a 7 m thick wackestone to packstone interval (particle sizes well above 30
177 microns meters and often rather millimeters to centimeters). In some places, the mudstone beds
178 are intercalated with few centimeters thick brownish silty marls (Fig. 2d). Such silty marls can
179 also reached 1 m thick at the base of the studied section. The top of the section ends with a 3 m

thick marly interval including sandy-carbonate beds. The complete sedimentary succession does not display any particular depositional architecture nor sedimentary structures. The main study section is located down West of the 3 km long exposure along the highway, where the carbonate beds only dip of 25-35° which permits to make measurements (Fig. 2a). A second section is located to the East, at the close vicinity of the Montpellier thrust and the Oligocene La Boissière normal fault (Fig. 2a). This second outcrop of "Lutetian" limestone strata is separated by map-scale strike-slip sinistral faults and cannot be precisely correlated to the whole outcrop as no benchmark beds is observed from both sections.

In thin section, the matrix of mudstones is composed of an unclear micrite sometimes including initially mud-size crushed bioclastic debris and peloids. The SEM image from 3D samples show micritic euhedral crystals of calcite less than 5 μm in size and few crystals of dolomite (less than 5%) (Fig. 3a). The present-day porosity of the studied mudstones, measured in laboratory on 11 mini cores using the triple weighting method, ranges from 4.4% to 22.3%. These mudstones are therefore qualified as fine-grained and porous carbonate rocks. The dark and homogeneous images from cathodoluminescence microscopy analysis reveal no difference between calcite grains and interstitial cements. We note that the imbricated contacts between calcite particles are observed at microscale disseminated in the material (Fig. 3b). The bed surfaces are affected by pedogenic modifications (i.e. desiccation cracks, micro-karstification, brecciation, iron oxide deposits…) related to shallow palustrine environments (wetlands), and therefore to common exposition to drying conditions and evaporative/groundwater recharge phases (Freytet and Plaziat, 1982; Alonso-Zarza and Wright, 2010). The mudstone beds of the second (eastern) outcrop show less evidences of emersion and contain several brecciated beds with higher quartz grains fraction. These specificities suggest a formation of this sedimentary section in a lacustrine

domain rather than palustrine environment, or at least a deeper water "lake" setting that records less the evaporative phases compared to the wetland environment of carbonate section of the western outcrop.

4. Description of faults

Different fault sets are observed along the study outcrop. We focus on meter-scale faults showing specific slickensides (see description section 4.2.) whereas Late Pyrenean or Oligocene fault networks (i.e. faults of several meters to tens meters length, cutting across the whole observable limestone section, with a brecciated fault core, a damage zone with mode I joint systems and calcite fiber along their surface) are not considered in the present study. Studied faults are organized in two different sets: a set of dip-slip normal faults at low-angle with respect to bedding, and a set of strike-slip faults at high-angle to bedding.

4.1. Location of faults within the limestone succession

Faults are heterogeneously distributed in the limestone succession. They affect almost all beds within the first 30 m and the last third of the mudstone sequence from 82 to 88 m (Fig. 4). They are mainly absent from 55 m to 75 m, especially in the wackestone-packstone interval. These faults are also observed restricted to specific mudstone beds that are intercalated within beds unaffected by faults from 30 to 55 m and from 75 to 82 m. The faults are only observed in limestone beds thicker than 20 cm (mainly absent in thinner ones). They can be observed whatever the secondary alteration occurring in affected limestone beds during syn-sedimentary subaerial exposure (desiccation, oxidation…) (Fig. 4). However, we note that faults are more

225 abundant in limestone beds showing few secondary alteration (for example the 2 m to 17 m
226 section) whereas they are mainly absent in highly altered limestone beds (for example the 55 m to
227 75 m section).

228

229 *4.2. Specificity of fault slickensides*

230 The studied faults differ from other fault systems affecting the limestone sections in the area by
231 their morphology and slickenside characteristics (Fig. 5). At the first order, these faults are
232 characterized by the lack of a macroscopic fault core (i.e. fault rock visible at the naked eyes) and
233 the lack of calcite or iron oxide precipitation along their slickensides (Fig. 5a). The slickensides
234 show grooves as frequent as ridges along the fault planes. These grooves and ridges features are
235 of several centimeters length and show U-shape with flat bottom (or flat top) and larger wave
236 length than amplitude (Figs. 5b, c). These grooves are observed at two imbricated scales of
237 width: 1 cm and 100s μm (Figs. 5b, e). The ridges of one wall of the fault plane perfectly fit into
238 the grooves of the other wall, i.e. no fracture porosity or cementation is observed along the fault
239 surface. These grooves show no specific asperity at the lower tip whereas two different
240 morphologies are observed at the upper tip of the groove: (1) V "crescentic" markings and (2)
241 step markings formed by sharp mm to cm-high plane, at high angle to the slickenside (following
242 the classification of Doblas, 1998) (Figs. 5b, c, d and f). These step markings are irregular planes
243 of centimeter to several centimeters length (Fig. 5d). They are uncommonly related to joint below
244 the fault plane but are more generally observed without associated deformation structures. No
245 stylolitic teeth are observed on these step markings.

246

247 *4.3. Normal fault system*

248 The low-angle to bedding faults are generally composed of meter-scale length structures (Fig.
249 6a). These faults are mainly restricted within single carbonate beds, and rarely affecting 2 or 3
250 beds. They show a sigmoidal shape (or flat S-shape) in cross-section with a maximum dip in the
251 central part of the beds, progressively decreasing at the top and base of the beds (listric to bed
252 interface) (Figs. 6b, c). Laterally, they form curved and irregular bended surfaces and show
253 connections with surrounding faults. The steps at the upper tip of the grooves along the
254 slickensides suggest a normal-sense kinematic (Petit & Laville 1987) (Fig. 5), but no offset
255 markers or tip folding are observable. These faults form a conjugate system with opposite dip.
256 After restoration to horizontal, stereographic plots reveal East-West oriented conjugate fault
257 system, with mainly North-South slickenlines (grooves) (Fig. 7a). Each dipping set is
258 crosscutting the other with a dominant observation of South-dipping set cutting the North-dipping
259 one (Figs. 6d, e). These crosscutting zones uncommonly show millimeter-scale normal-sense
260 shear-displacement but no measurable offset is more generally detected along these faults.
261 Moreover, numerous abutting contacts are observed between both sets (Fig. 6d, e). Few NW or
262 SW-striking slickenlines are also measured. The dip of the faults, measured systematically in the
263 central part of beds, is on average 25° ± 7°, suggesting a high dihedral angle of about 130°
264 between conjugate fault sets (Fig. 7b). The rake data show purely dip-slip motion (Fig. 7c).

265

266 *4.4. Strike-slip fault system*

267 The high-angle to bedding faults show large grooves and ridges similarly to low-angle normal
268 faults (Figs. 8a, b). These faults generally cross-cut several limestone layers (2 to 5 beds). They

show numerous centimeter-scale dilational jogs between meter-scale planar fault segments (Fig. 8c). These dilational jogs observed along the fault revealed a shear-displacement of about 1 cm (Fig. 8d). These faults form then a strike-slip system with a dextral set of strike ranging of strike ranging from N°20E to N°50E and a sinistral set striking from N°150E to N°180E (Fig. 9a). The strike-slip faults form a conjugate system with a general dihedral angle between 120° and 140° (similarly to the normal-sense set). These faults are almost vertical after restoration of bedding to horizontal, on average 79° ± 9°, and show mostly horizontal slickenlines (grooves) with a plunge of 11° ± 13° on average (both North or South) (Fig. 9b) and a rake around the 0° and the 180° values (i.e. horizontal) (Fig. 9c).

The strike-slip fault systems generally cross-cut the normal-sense fault system (Fig. 8a), but, a same surface is sometimes observed as laterally evolving from strike-slip to dip-slip slickensides, with a progressive decrease of dip and showing parallel grooves of similar trend (Figs. 10a, b). We note that both dip-slip and strike-slip systems are commonly observed together (Fig. 10d). However, a bed-by-bed analysis of fault system within the first 47 beds of the limestone succession reveals 6 beds where only dip-slip normal faults are observed and 3 beds with only strike-slip faults (Fig. 10c). The fault spacing of only few tens centimeters revealed a pervasive distribution of both sets in bed affected by faulting (Fig. 10d). We note that several examples of strike-slip slickensides are observed along the plane of late strike-slip brittle faults (i.e. faults of tens meters length, with a brecciated fault core and calcite fiber along the fault mirror).

4.5. Microstructure of faults

290 The microstructure of the limestone in the wall along the fault plane changes from areas where
291 the grain framework is similar to the host rock (grain size, shape, composition, porosity) into
292 zones where the microporosity is significantly reduced close to the main fault surface (Fig. 11).
293 The thickness of this low-porosity zone is variable and can reach in the best-case 0.3 mm below
294 the fault plane. These compacted zones are preferentially observed at fault plane irregularities,
295 i.e. where small dip changes occurs and forms compressive jogs along the slickenside (Figs. 11a,
296 c, d). This specific location of compaction is consistent with the kinematics of the faults deduced
297 form field observations. Smooth pressure-solution seams are observed particularly in these zones
298 as sinuous cleavages following grain contacts (Figs. 11c, d). These cleavages are parallel or
299 slightly oblique to the faults and are sometimes open (probably related to thin-section
300 preparation). Concerning step markings located at the upper tip of the groove, these areas show
301 no evidence of compaction. The presence of dilation joint is sometimes observed (Fig. 11e), but
302 several examples show no deformation feature below the step. A sharp plane penetrating the
303 material is often observed in the continuity of the fault plane and could be interpreted as P plane
304 structure (Fig. 11e). No significant grain orientation is observed in the host material (Fig. 12a).
305 However, compacted areas show a preferential orientation of grains parallel to the fault plane
306 (Figs. 12b, c).

307 A low-porosity and compacted zone of few tens of micrometers is observed above the main fault
308 plane (Fig. 11b). In this zone, the particles appear smaller than the ones of host material (Fig.
309 13a). We note that only few grains with microcracks and no hertzian contacts were identified in
310 these structures. This zone is bordered by the main fault slickenside. Several tens μm long planes
311 are also observed within the comminuted zone (Fig. 11b). This comminution is accompanied by a
312 crystallographic preferred orientation (CPO) of grains as revealed by the dominant reddish color

313 of grains within the compacted fault zone (EBSD acquisition showing colors depending on the
314 crystallographic organization of each grains) (Fig. 13a). This CPO shows a maximum *m.u.d.*
315 value of 4.85 whereas this value nether exceeds 1.70 in the host rock (Fig. 13b). This CPO is
316 observed in the c-axis of calcite grains and is oriented about 70° to the fault plane. We note that
317 twining process is revealed by µm-thick bands showing a different color than the grain they
318 affect (Fig. 14a). These twins are only observed within the compacted area of the fault core or the
319 compactive jogs (Figs. 14b, c) whereas no twins are observed on step marking at the upper tip of
320 grooves (Fig. 14d). This specific location of calcite twins is consistent with the normal-sense
321 kinematic proposed for the fault system at low-angle dip relative to the bedding.

322

323 *4.6. Fault slip and stress analysis*

324 Strike directions of faults are clustered East-West and rakes have 3 modes: a major mode that is
325 pure normal (rake around -90, Fig. 7c) and two minor modes, around pure sinistral (left lateral)
326 and pure dextral (right lateral) (rake around 0 and 180, Fig. 9c). Inverting the restored dataset and
327 taking into account all of the 264 data yields a solution with only three outliers with a rake misfit
328 larger than 160°. This can be due either to discordant movements or to erroneous slip sense
329 determination. It was thus decided to invert for 99% of the data to disable any influence of the
330 outliers on the result. The resulting solution is at the transition between extensional and wrench
331 regime with $\mathbf{s}_3$ horizontal and about N°10E (Fig. 15a). In this solution, $\boldsymbol{s}_1$ is vertical and show a
332 very close value with $\mathbf{s}_2$ suggested by the $r_0 = 0.0$. This solution also yields a low average angular
333 error (<10°, computed on 99% of the data), a large number of faults with rake misfit below 15°
334 ($N_{exp15} = 216$), and the highest value *InvQual* = 2 (Fig. 15b). The normal faults are at high angle

335 ($\geq 60°$) with $\mathbf{s}_1$ because of their low (15-30°) dip with respect to bedding. The strike-slip faults
336 are also at high angle with $\mathbf{s}_2$, which plays the same role as $\mathbf{s}_1$ when $r_0 = 0.0$. As a consequence
337 both types of fault data are located on the right hand side of Mohr's circle (Fig. 15c). The quality
338 of the solution supports the fact that all faults are dynamically consistent.

339

340 **5. Multi-beds normal faults**

341 Several multi-beds normal faults (i.e. non-stratabound faults) are observed at the second studied
342 site, eastward of the main study outcrop (Fig. 2a). Because of the specificity of these structures
343 and their absence in the main 2.5 km long outcrop, we decided to describe them separately.

344 Slickensides of the multi-beds normal-faults show closely similar morphology than the bed-
345 restricted faults, i.e. grooves and ridges, marking steps, no calcite precipitation, and curved planes
346 (Fig. 16a). The specificity of such slickensides is the presence of visible indentations at lower tip
347 of grooves interpreted as slickolites (i.e. sheared pressure-solution zone, Arthaud and Mattauer,
348 1969) (Fig. 16b). The height of these faults is at least 10 m and their horizontal length is about
349 several tens of meters. They are mainly trending EW and dip exclusively to the South (Fig. 16c).
350 Their average dip is 23° ± 7° (after bedding restored to horizontal). The fault throw can reach few
351 centimeters (Fig. 16d, see the evidence of footwall bed marks on the fault slickenside). We note
352 evidences of reactivation in reverse-sense motion on one of these faults, i.e. fine and regular
353 striation oblique to the main normal slickenlines, consistently with a reactivation during late
354 Eocene Pyrenean shortening. No multi-bed normal fault dipping to the North was observed at this
355 site. Brittle-like (late) strike-slip structures are observed with brecciated fault core, calcite fiber

356 along the fault plane, and mode I fracture damage zone (joints), but no strike-slip slickensides
357 were clearly identified.

358

359 **6. Discussion**

360 *6.1. Model of fault formation*

361 The low intergranular porosity zones having wavy cleavage observed close to the fault planes
362 (Fig. 11), the comminution, CPO and twinning observed in the fault core, as well as the high
363 dihedral angle between conjugate faults (130° to the shortening axis) reveals that the deformation
364 mechanism is hybrid between compaction and shear, and not controlled by a standard Coulomb
365 type frictional strength law. These characteristics expressing failure on the right hand side of the
366 Mohr's circle (Fig. 15c) are consistent with shear-enhanced compaction and pore collapse modes
367 observed in porous granular material having yield envelope with elliptical end cap (Wong and
368 Baud, 2012; Cilona et al., 2014) (Fig. 17a). Indeed, studied limestones are composed of micritic
369 grains of calcite with relatively high interstitial porosity (up to 22%; we note that these faults are
370 very rarely or never observed in wackestone or packstone carbonate beds). They probably
371 behaved similarly to other porous and fine granular carbonates such as chalk (Risnes, 2001;
372 Risnes et al., 2005) or marine limestones (Vajdova *et al.* 2004; Wong & Baud 2012 and
373 references therein). The size of such yield envelopes is mainly controlled by the porosity and the
374 grain size of the host material (if grain fragmentation is involved) as well as particle cementation
375 (e.g. Estrada and Taboada 2013; Soliva *et al.* 2013). This mechanical model implies that the
376 faults were formed along the cap under low ratios between applied shear and normal stress (Fig.
377 17a).

The stress state leading to fault formation can be obtained under a progressive increase of burial with a high coefficient of Earth pressure at rest (K_0 the ratio of vertical to horizontal stresses in oedometric conditions, i.e. no horizontal remote stress). This ratio ranges from 0.5 to 1 in very fine-grained materials (Goulty 2003; Mitchell & Soga 2005) but is not constrained for continental unlithified micritic carbonate muds to your knowledge. The occurrence of both sub-synchronous normal-sense and strike-slip systems suggests that vertical (σ_v) and horizontal (σH_{EW}) stresses are very close. This fault pattern and the occurrence of faults in an unconsolidated material argue for a high K_0 context since no evidence of EW regional (tectonic) contraction is observed in this area. We here consider a range of K_0 from 0.7 to 0.9 to estimate stress paths leading to faults formation (Fig. 17a). All these observations and mechanical considerations allow considering these faults as formed by burial driven compaction during the increase of burial depth. The presence of faults within the top of the sequence suggests that structures can form under a burial of only few tens meters depth (Fig. 4). Their curved and irregular geometry is consistent with subsurface conditions of formation in poorly lithified rocks (Guiraud and Séguret, 1987). We note that faults are generally observed in the limestone succession showing less evidences of subaerial exposure (karstification, desiccation…) (Fig. 4). Subaerial exposure, by its impact on the host material rheology, would probably prevent the formation of such faults.

However, it is not common to localize shear plane in such mechanical context favourable to compaction banding with more or less shear component (Schultz and Siddharthan, 2005; Baud et al., 2006; Soliva et al., 2013). In these cited examples, the compaction and the pore collapse mainly occurred by cataclasis, leading to pervasive network of compactive cataclastic bands (Solum et al., 2010; Saillet and Wibberley, 2010; Ballas et al., 2015; Soliva et al., 2016; Cavailhes and Rotevatn, 2018; Robert et al., 2018) and uncommonly conduct to shear plane

401 localization following the strain hardening model of Aydin and Johnson (1978) (e.g. Rotevatn et
402 al., 2008; Tueckmantel et al., 2010). The fault mechanism described in the present study differs
403 from this model of localization as a combination of processes is involved, i.e. grain rotation,
404 pressure-solution, comminution, and a dynamic recrystallization as revealed by the
405 crystallographic preferred orientation (CPO) of grains (Smith et al., 2013; Delle Piane et al.,
406 2017). By this way, it is interesting to compare the characteristics of these planes to the
407 slickensides described in C-S structures in crystalline rocks at the deep brittle-ductile transition
408 (Berthé et al., 1979; Lin et al., 2007). In such contexts, slickensides share similar characteristics
409 than the presently studied structures: grooves and ridges morphology without noticeable down-
410 slip ends, and slickenlines (grooves) of several centimeters length for a fault of cm-scale shear-
411 displacement (e.g. Means, 1987). To explain this strain localization in a ductile context, a plastic
412 behaviour of material which is not related to a frictional sliding process is proposed by Lin and
413 Williams (1992). As expressed by Will and Wilson (1989) from analog laboratory experiments:
414 "the excess length and the nesting between footwall and hanging wall ridges and grooves is
415 therefore a product of this plastic deformation".

416 We propose that quite similar hybrid and evolving processes occurred under sub-surface
417 conditions in response of plastic processes followed by shear localization and an early blocking
418 of the fault movement. The fault initiation starts by disaggregation and grain comminution within
419 10s μm thick zones (Fig. 17b, stage 1). The process triggering the grain comminution remains
420 unclear. No evidence of significant cataclasis was observed even if this process cannot be totally
421 excluded. However, the grain comminution is accompanied by a dynamic recrystallization of
422 calcite as revealed by the CPO within the comminuted zone. The potential hardening induced by
423 the grain comminution (Schultz and Siddharthan, 2005; Wibberley et al., 2007) evolves

424 contemporaneously with a softening behaviour induced by the dynamic recrystallization (Smith
425 et al., 2013), which conducts to shear localization. This shear localization seems initiated by
426 segments of hundreds μm to several mm long, and is developed within or, more frequently, along
427 the comminuted-recrystallized zone (Fig. 17b, stage 2). We note that grain rotation and pressure-
428 solution evidences are generally observed within compressive jogs and are not observed all along
429 the fault plane. This specific location suggests that these processes acts as secondary mechanisms
430 related to the fault plane heterogeneities and then mainly occurred after the fault localization (Fig.
431 17b, stage 3). However, these processes reveal a compactive behaviour during the last stage of
432 the fault evolution which certainly triggers an early blocking of the fault movement as expressed
433 by the very low shear displacement measured along the fault slickensides.

434 The formation of two sub-synchronous conjugate systems rather than radial or random patterns is
435 quite unexpected considering that this mechanism of faulting is triggered by compaction and
436 burial context. This particularity in the fault pattern can be explained by a decrease of the NS (σ_3)
437 stress induced by the syn-burial tilting of sedimentary layers since they are located in the extrados
438 of a very smooth antiform associated with the flexure of the foreland basin (foreland bulge, Fig.
439 17c) (e.g. Ferrill et al., 2021). In this particular setting, a conjugate system of E-W oriented
440 normal-sense faults formed consistently with the polarization of horizontal stresses (NS s_3),
441 impeding more random pattern formation. The strike-slip faults generally crosscut the low-angle
442 normal faults whereas their connection may be a local reactivation of the normal system. The
443 strike-slip system could then initiate slightly later, consistently with a close value of σ_1 and σ_2
444 (Morris and Ferrill, 2009), and could be linked to local stress release induced by the formation of
445 the normal-sense system. More precisely, the softening occurring during the shear plane
446 localization of normal-sense faults could be enough to imply simultaneously the permutation

447 between a vertical s_1 to a horizontal and East-West s_1 (local stress perturbation due to fault slip),
448 especially if we considered a high K_0 value. We underline that the similarity between dihedral
449 angles for both the strike-slip and normal fault sets (130°), suggests that the material had the
450 same behaviour during normal faulting and strike-slip faulting, and also that no significant
451 vertical compaction occurred after fault formation (i.e. vertical compaction would have only
452 increased the dihedral angle between normal faults). This observation suggests that the material
453 reaches its maximum mechanical compaction during the development of the studied faults.

454 The occurrence of fault sets within specific beds or beds section of the limestone succession (Fig.
455 4) suggests that additional factors affect the fault formation. Low-porosity and/or early
456 cementation as well as the rock texture (distribution of grain size and nature of grains) in beds
457 may certainly impede the initiation of such hybrid compactive faults, similarly to the well-known
458 conditioning parameters described for deformation bands occurrence in porous sandstones
459 (Fossen et al., 2018a and references therein). Moreover, external larger-scale factors such the
460 sedimentation rate controlling the overloading stress or the tectonic features (tilting and slope,
461 regional stresses) can also periodically create favourable or unfavourable conditions for fault
462 initiation.

463

464 *6.2. The specific case of multi-beds faults*

465 The specificity of multi-beds faults remains elusive. Most of their characteristics argue for a
466 similar mechanical context of formation by compaction processes, under the influence of a NS
467 trending s_3. These multi-beds faults cannot be considered as the evolution of bed-restricted ones
468 as their slickensides show any evidences of segment connection and cut across several limestone

beds without marked plan bending. We propose that these multi-beds faults formed in an area of higher sedimentation rate consistently with the lack of significant emersion and the presence of several sedimentary breccias (debris flow from the thrust relief). This higher sedimentation rate coupled with less marked mechanical stratigraphy (fewer differences between rheology of limestone beds compared to more fluctuating palustrine environment) is proposed to explain the occurrence of such large-scale slickensides. The apparent absence of the conjugate set is also interpreted to be linked with a larger influence of the slope during fault formation. We note that these faults are not significantly reactivated during late Eocene Pyrenean shortening despite of their EW orientation and their location in front of the main thrust system. This suggests that these faults, from their deformation mechanisms, morphology, and diagenetic origin, are not suitable to form preferential plane of weakness.

6.3. Comparison with other fault systems

Other fault systems share several geometrical attributes with the fault system described in the present study. For example, distributed patterns of compactive faults have already been described as cataclastic shear-enhanced compaction bands in porous sandstones (Eichhubl et al., 2010; Ballas et al., 2013; Fossen et al., 2015) and porous limestones (Rustichelli et al., 2012; Rotevatn et al., 2016; Kaminskaite et al., 2019), or as deformation bands with particles reorientation-torsion in clayey materials (Ujiie et al., 2004; Milliken and Reed, 2010). Furthermore, meter-scale shear structures showing both cataclasis and pressure-solution were described in porous limestones (Tondi et al., 2006; Rotevatn et al., 2016; Tavani et al., 2018b), chalk (Kaminskaite et al., 2019) or undetermined carbonate (Marshak et al., 1982). These examples and the fault system

491 described in the present study complete the range of localized deformation structures observed
492 along end cap yield envelop of porous materials (Fossen et al., 2018b; Ferrill et al., 2021).
493 However, these cited examples of pervasive compactional structures differ from our fault system
494 as there are mainly deformation bands without localization of slickensides and they are mainly
495 related to regional contractional stress fields.

496 Compaction of sediment during burial conditions is mainly diffuse across the entire material
497 (Ehrenberg and Nadeau, 2005). The compaction can also take place in discontinuity such as bed-
498 parallel pressure-solution seams (Toussaint et al., 2018; Meng et al., 2021) or compaction bands
499 (Tondi et al., 2006; Aydin and Ahmadov, 2009). However, the participation of shear
500 discontinuities in the sediment compaction remains mainly not considered although polygonal
501 fault patterns observed worldwide in offshore sediments (Cartwright et al., 2003; Gay et al.,
502 2004; Cartwright, 2011; Gay, 2017) are discussed to be triggered during sediment burial and
503 diagenesis. In chalks, Hibsch et al., (2003) described polygonal faulting where shearing is
504 associated with decrease of porosity by pressure solution and cementation. Conversely,
505 Wennberg et al., (2013) described cataclastic compaction bands triggered by vertical loading
506 during burial (no information of the fault pattern). In our study, faults appear to be a hybrid
507 system between these two previously cited examples as cataclasis, pressure-solution and dynamic
508 recrystallization is observed.

509 We note that the polygonal faults described by Tewksbury et al. (2014) show calcite
510 mineralization along the fault plane which implies a dominant dilatant behaviour. The meter-
511 scale compactive normal faults described by Guiraud and Séguret, (1987) in clayey sediments are
512 also related to water-escape structures during sediment compaction (their low-angle to bedding
513 and their slickenside morphology are quite similar to our study faults). These examples reveal

514 that different micro-mechanisms can occur within the shear discontinuities initiated during
515 sediment compaction. These structures participate to sediment compaction by compactive
516 mechanisms within the shear structures (cataclasis, pressure-solution) or by dilatant behaviour
517 which permits fluid expulsion and diffuse compaction of the host material.

518

519 **7. Conclusion**

520 Compactive faults showing hybrid micromechanisms of deformation are described in micritic
521 porous limestones from the South of France. These faults are organized in distributed patterns of
522 meter-scale structures and form two sub-synchronous conjugate sets: a set composed of low-
523 angle normal faults and a set composed of subvertical strike-slip faults. Their curve plane,
524 incipient shear offset, high angle relative to s_1, and porosity reduction argues for a dominant
525 compaction behaviour during faulting. Comminution, dynamic recrystallization (revealed by the
526 crystallographic preferred orientation from EBSD acquisitions), pressure-solution and grain
527 rotation are observed in these structures initiated during early sediment burial and basin flexure.
528 These faults complete the range of compactive structures formed along the end cap yield envelop
529 of porous materials. This example underlines the complexity of deformation processes occurring
530 under compaction and early burial context, especially in such poorly consolidated carbonate
531 material.

532

533 **Acknowledgements**

We acknowledge Pierre Azémard, Patrick Demange, Jean-Christophe Merzeau and all the team from CEI Montarnaud to give us access and support along A750 Highway. We are grateful to Doriane Delmas and Christophe Nevado for the high quality thin-sections and, Frédéric Fernandez and Fabrice Barou for the help on the SEM and EBSD devices. We also thank Michel Lopez, Alfredo Taboada, and Didier Loggia for constructive discussions about the fault formation. We acknowledge Andrea Billi and David Ferrill for their constructive reviews which improve the manuscript.

Funding information

This work relied on basic support from the Geosciences Montpellier Laboratory and on the Tellus Program of CNRS/INSU.

References

Agosta, F., Alessandroni, M., Tondi, E., Aydin, A., 2010. Oblique normal faulting along the northern edge of the Majella Anticline, central Italy: Inferences on hydrocarbon migration and accumulation. Faulting and Fracturing of Carbonate Rocks: New Insights into Deformation Mechanisms, Petrophysics and Fluid Flow Properties 32, 1317–1333. https://doi.org/10.1016/j.jsg.2010.10.007

Agosta, F., Aydin, A., 2006. Architecture and deformation mechanism of a basin-bounding normal fault in Mesozoic platform carbonates, central Italy. Journal of Structural Geology 28, 1445–1467. https://doi.org/10.1016/j.jsg.2006.04.006

Agosta, F., Ruano, P., Rustichelli, A., Tondi, E., Galindo-Zaldívar, J., Sanz de Galdeano, C., 2012. Inner structure and deformation mechanisms of normal faults in conglomerates and carbonate grainstones (Granada Basin, Betic Cordillera, Spain): Inferences on fault permeability. Fault Zone Structure, Mechanics and Evolution in Nature and Experiment 45, 4–20. https://doi.org/10.1016/j.jsg.2012.04.003

Alabouvette, B., Aubague, M., Bambier, A., Feist, R., Paloc, H., 1982. Carte géologique de Lodève., scale 1/50 000.

Alonso-Zarza, A.M., Wright, V.P., 2010. Chapter 2 Palustrine Carbonates. In: Alonso-Zarza, A.M., Tanner, L.H. (Eds.), Developments in Sedimentology. Elsevier, 103–131. https://doi.org/10.1016/S0070-4571(09)06102-0

Angelier, J., 1984. Tectonic analysis of fault slip data sets. Journal of Geophysical Research: Solid Earth 89, 5835–5848. https://doi.org/10.1029/JB089iB07p05835

Antonellini, M., Aydin, A., 1995. Effect of Faulting on Fluid Flow in Porous Sandstones: Geometry and Spatial Distribution1. AAPG Bulletin 79, 642–671. https://doi.org/10.1306/8D2B1B60-171E-11D7-8645000102C1865D

Antonellini, M., Aydin, A., 1994. Effect of Faulting on Fluid Flow in Porous Sandstones: Petrophysical Properties1. AAPG Bulletin 78, 355–377. https://doi.org/10.1306/BDFF90AA-1718-11D7-8645000102C1865D

Antonellini, M., Petracchini, L., Billi, A., Scrocca, D., 2014. First reported occurrence of deformation bands in a platform limestone, the Jurassic Calcare Massiccio Fm., northern Apennines, Italy. Tectonophysics 628, 85–104. https://doi.org/10.1016/j.tecto.2014.04.034

Arthaud, F., Mattauer, M., 1969. Exemples de stylolites d'origine tectonique dans le Languedoc, leurs relations avec la tectonique cassante. Bulletin de La Société Géologique de France S7-XI, 738–744. https://doi.org/10.2113/gssgfbull.S7-XI.5.738

Arthaud, F., Séguret, M., 1981. Les structures pyrénéennes du Languedoc et du Golfe du Lion (Sud de la France). Bulletin de La Société Géologique de France S7-XXIII, 51–63. https://doi.org/10.2113/gssgfbull.S7-XXIII.1.51

Aydin, A., 2006. Failure modes of the lineaments on Jupiter's moon, Europa: Implications for the evolution of its icy crust. Faulting and Fault-Related Processes on Planetary Surfaces 28, 2222–2236. https://doi.org/10.1016/j.jsg.2006.08.003

Aydin, A., Ahmadov, R., 2009. Bed-parallel compaction bands in aeolian sandstone: Their identification, characterization and implications. Tectonophysics 479, 277–284. https://doi.org/10.1016/j.tecto.2009.08.033

Aydin, A., Johnson, A.M., 1978. Development of faults as zones of deformation bands and as slip surfaces in sandstone. Pure and Applied Geophysics 116, 931–942. https://doi.org/10.1007/BF00876547

Ballas, G., Fossen, H., Soliva, R., 2015. Factors controlling permeability of cataclastic deformation bands and faults in porous sandstone reservoirs. Journal of Structural Geology 76, 1–21. https://doi.org/10.1016/j.jsg.2015.03.013

Ballas, G., Soliva, R., Benedicto, A., Sizun, J.-P., 2014. Control of tectonic setting and large-scale faults on the basin-scale distribution of deformation bands in porous sandstone (Provence, France). Fluid-Rock-Tectonics Interactions in Basins and Orogens 55, 142–159. https://doi.org/10.1016/j.marpetgeo.2013.12.020

Ballas, G., Soliva, R., Sizun, J.-P., Fossen, H., Benedicto, A., Skurtveit, E., 2013. Shear-enhanced compaction bands formed at shallow burial conditions; implications for fluid flow (Provence, France). Journal of Structural Geology 47, 3–15. https://doi.org/10.1016/j.jsg.2012.11.008

Balsamo, F., Clemenzi, L., Storti, F., Mozafari, M., Solum, J., Swennen, R., Taberner, C., Tueckmantel, C., 2016. Anatomy and paleofluid evolution of laterally restricted extensional fault zones in the Jabal Qusaybah anticline, Salakh arch, Oman. GSA Bulletin 128, 957–972. https://doi.org/10.1130/B31317.1

Baud, P., Vajdova, V., Wong, T., 2006. Shear-enhanced compaction and strain localization: Inelastic deformation and constitutive modeling of four porous sandstones. Journal of Geophysical Research: Solid Earth 111. https://doi.org/10.1029/2005JB004101

Berthé, D., Choukroune, P., Jegouzo, P., 1979. Orthogneiss, mylonite and non coaxial deformation of granites: the example of the South Armorican Shear Zone. Journal of Structural Geology 1, 31–42. https://doi.org/10.1016/0191-8141(79)90019-1

Billi, A., 2005. Grain size distribution and thickness of breccia and gouge zones from thin (<1m) strike-slip fault cores in limestone. Journal of Structural Geology 27, 1823–1837. https://doi.org/10.1016/j.jsg.2005.05.013

612 Billi, A., 2003. Solution slip and separations on strike-slip fault zones: theory and application to the
613 Mattinata Fault, Italy. Journal of Structural Geology 25, 703–715. https://doi.org/10.1016/S0191-
614 8141(02)00077-9
615 Bonnet, A., Andrieux, J., Mattauer, M., Coubes, L., Paloc, H., 1971. Notice de la carte géologique à 1/50
616 000, feuille Montpellier, 2nde édition. 29.
617 Bott, M.H.P., 1959. The Mechanics of Oblique Slip Faulting. Geological Magazine 96, 109–117.
618 https://doi.org/10.1017/S0016756800059987
619 Bullock, R.J., De Paola, N., Holdsworth, R.E., Trabucho-Alexandre, J., 2014. Lithological controls on the
620 deformation mechanisms operating within carbonate-hosted faults during the seismic cycle.
621 Journal of Structural Geology 58, 22–42. https://doi.org/10.1016/j.jsg.2013.10.008
622 Burg, J.-P., Célérier, B., Chaudhry, N.M., Ghazanfar, M., Gnehm, F., Schnellmann, M., 2005. Fault analysis
623 and paleostress evolution in large strain regions: methodological and geological discussion of the
624 southeastern Himalayan fold-and-thrust belt in Pakistan. Journal of Asian Earth Sciences 24, 445–
625 467. https://doi.org/10.1016/j.jseaes.2003.12.008
626 Bussolotto, M., Benedicto, A., Moen-Maurel, L., Invernizzi, C., 2015. Fault deformation mechanisms and
627 fault rocks in micritic limestones: Examples from Corinth rift normal faults. Journal of Structural
628 Geology 77, 191–212. https://doi.org/10.1016/j.jsg.2015.05.004
629 Cartwright, J., 2011. Diagenetically induced shear failure of fine-grained sediments and the development
630 of polygonal fault systems. Marine and Petroleum Geology 28, 1593–1610.
631 https://doi.org/10.1016/j.marpetgeo.2011.06.004
632 Cartwright, J., James, D., Bolton, A., 2003. The genesis of polygonal fault systems: a review. Geological
633 Society, London, Special Publications 216, 223. https://doi.org/10.1144/GSL.SP.2003.216.01.15
634 Cavailhes, T., Rotevatn, A., 2018. Deformation bands in volcaniclastic rocks – Insights from the Shihtiping
635 tuffs, Coastal Range of Taiwan. Journal of Structural Geology 113, 155–175.
636 https://doi.org/10.1016/j.jsg.2018.06.004
637 Célérier, B., 2020. FSA: Fault & Stress Analysis software.
638 Cilona, A., Baud, P., Tondi, E., Agosta, F., Vinciguerra, S., Rustichelli, A., Spiers, C.J., 2012. Deformation
639 bands in porous carbonate grainstones: Field and laboratory observations. Fault Zone Structure,
640 Mechanics and Evolution in Nature and Experiment 45, 137–157.
641 https://doi.org/10.1016/j.jsg.2012.04.012
642 Cilona, A., Faulkner, D.R., Tondi, E., Agosta, F., Mancini, L., Rustichelli, A., Baud, P., Vinciguerra, S., 2014.
643 The effects of rock heterogeneity on compaction localization in porous carbonates. Journal of
644 Structural Geology 67, 75–93. https://doi.org/10.1016/j.jsg.2014.07.008
645 Clemenzi, L., Molli, G., Storti, F., Muchez, P., Swennen, R., Torelli, L., 2014. Extensional deformation
646 structures within a convergent orogen: The Val di Lima low-angle normal fault system (Northern
647 Apennines, Italy). Journal of Structural Geology 66, 205–222.
648 https://doi.org/10.1016/j.jsg.2014.05.019
649 Crider, J.G., Peacock, D.C.P., 2004. Initiation of brittle faults in the upper crust: a review of field
650 observations. Journal of Structural Geology 26, 691–707.
651 https://doi.org/10.1016/j.jsg.2003.07.007
652 Debrand-Passard, S., Courbouleix, S., Lienhardt, M.-J., 1984. Synthèse géologique du Sud-Est de la
653 France. Éditions du Bureau de recherches géologiques et minières.
654 Delle Piane, C., Clennell, M.B., Keller, J.V.A., Giwelli, A., Luzin, V., 2017. Carbonate hosted fault rocks: A
655 review of structural and microstructural characteristic with implications for seismicity in the
656 upper crust. Journal of Structural Geology 103, 17–36. https://doi.org/10.1016/j.jsg.2017.09.003
657 Demurtas, M., Smith, S.A.F., Prior, D.J., Spagnuolo, E., Di Toro, G., 2019. Development of crystallographic
658 preferred orientation during cataclasis in low-temperature carbonate fault gouge. Journal of
659 Structural Geology 126, 37–50. https://doi.org/10.1016/j.jsg.2019.04.015

660 Doblas, M., 1998. Slickenside kinematic indicators. Tectonophysics 295, 187–197.
661 https://doi.org/10.1016/S0040-1951(98)00120-6
662 Ehrenberg, S.N., Nadeau, P.H., 2005. Sandstone vs. carbonate petroleum reservoirs: A global perspective
663 on porosity-depth and porosity-permeability relationships. AAPG Bulletin 89, 435–445.
664 https://doi.org/10.1306/11230404071
665 Eichhubl, P., Hooker, J.N., Laubach, S.E., 2010. Pure and shear-enhanced compaction bands in Aztec
666 Sandstone. Structural Diagenesis 32, 1873–1886. https://doi.org/10.1016/j.jsg.2010.02.004
667 Estrada, N., Taboada, A., 2013. Yield surfaces and plastic potentials of cemented granular materials from
668 discrete element simulations. Computers and Geotechnics 49, 62–69.
669 https://doi.org/10.1016/j.compgeo.2012.11.001
670 Etchecopar, A., Vasseur, G., Daignieres, M., 1981. An inverse problem in microtectonics for the
671 determination of stress tensors from fault striation analysis. Journal of Structural Geology 3, 51–
672 65. https://doi.org/10.1016/0191-8141(81)90056-0
673 Ferraro, F., Grieco, D.S., Agosta, F., Prosser, G., 2018. Space-time evolution of cataclasis in carbonate
674 fault zones. Journal of Structural Geology 110, 45–64. https://doi.org/10.1016/j.jsg.2018.02.007
675 Ferrill, D.A., Evans, M.A., McGinnis, R.N., Morris, A.P., Smart, K.J., Wigginton, S.S., Gulliver, K.D.H.,
676 Lehrmann, D., Zoeten, E. de, Sickmann, Z., 2017. Fault zone processes in mechanically layered
677 mudrock and chalk. Journal of Structural Geology 97, 118–143.
678 https://doi.org/10.1016/j.jsg.2017.02.013
679 Ferrill, D.A., Morris, A.P., 2003. Dilational normal faults. Journal of Structural Geology 25, 183–196.
680 https://doi.org/10.1016/S0191-8141(02)00029-9
681 Ferrill, D.A., Smart, K.J., Cawood, A.J., Morris, A.P., 2021. The fold-thrust belt stress cycle: Superposition
682 of normal, strike-slip, and thrust faulting deformation regimes. Journal of Structural Geology 148,
683 104362. https://doi.org/10.1016/j.jsg.2021.104362
684 Ferrill, D.A., Smart, K.J., Morris, A.P., 2020. Fault failure modes, deformation mechanisms, dilation
685 tendency, slip tendency, and conduits v. seals. Geological Society, London, Special Publications
686 496, 75. https://doi.org/10.1144/SP496-2019-7
687 Fisher, Q.J., Knipe, R.J., 2001. The permeability of faults within siliciclastic petroleum reservoirs of the
688 North Sea and Norwegian Continental Shelf. Marine and Petroleum Geology 18, 1063–1081.
689 https://doi.org/10.1016/S0264-8172(01)00042-3
690 Fossen, H., Bale, A., 2007. Deformation bands and their influence on fluid flow. AAPG Bulletin 91, 1685–
691 1700. https://doi.org/10.1306/07300706146
692 Fossen, H., Schultz, R.A., Shipton, Z.K., Mair, K., 2007. Deformation bands in sandstone: a review. Journal
693 of the Geological Society 164, 755. https://doi.org/10.1144/0016-76492006-036
694 Fossen, H., Soliva, R., Ballas, G., Trzaskos, B., Cavalcante, C., Schultz, R.A., 2018a. A review of deformation
695 bands in reservoir sandstones: geometries, mechanisms and distribution. Geological Society,
696 London, Special Publications 459, 9. https://doi.org/10.1144/SP459.4
697 Fossen, H., Soliva, R., Ballas, G., Trzaskos, B., Cavalcante, C., Schultz, R.A., 2018b. A review of deformation
698 bands in reservoir sandstones: geometries, mechanisms and distribution. Geological Society,
699 London, Special Publications 459, 9. https://doi.org/10.1144/SP459.4
700 Fossen, H., Zuluaga, L.F., Ballas, G., Soliva, R., Rotevatn, A., 2015. Contractional deformation of porous
701 sandstone: Insights from the Aztec Sandstone, SE Nevada, USA. Journal of Structural Geology 74,
702 172–184. https://doi.org/10.1016/j.jsg.2015.02.014
703 Freytet, P., Plaziat, J.-C., 1982. Continental carbonate sedimentation and pedogenesis-Late Cretaceous
704 and Early Tertiary of southern France.
705 Gay, A., 2017. Are polygonal faults the keystone for better understanding the timing of fluid migration in
706 sedimentary basins? EPJ Web Conf. 140. https://doi.org/10.1051/epjconf/201714012009

Gay, A., Lopez, M., Cochonat, P., Sermondadaz, G., 2004. Polygonal faults-furrows system related to early stages of compaction – upper Miocene to recent sediments of the Lower Congo Basin. Basin Research 16, 101–116. https://doi.org/10.1111/j.1365-2117.2003.00224.x

Goulty, N.R., 2003. Reservoir stress path during depletion of Norwegian chalk oilfields. Petroleum Geoscience, 9, 233–241.

Graham, B., Antonellini, M., Aydin, A., 2003. Formation and growth of normal faults in carbonates within a compressive environment. Geology 31, 11–14. https://doi.org/10.1130/0091-7613(2003)031<0011:FAGONF>2.0.CO;2

Guiraud, M., Séguret, M., 1987. Soft-sediment microfaulting related to compaction within the fluviodeltaic infill of the Soria strike-slip basin (northern Spain). Geological Society, London, Special Publications 29, 123. https://doi.org/10.1144/GSL.SP.1987.029.01.11

Hartenberger, J.L., Sigé, B., Sudre, J., 1969. Les gisements de vertébrés de la région montpelliéraine. 1.-Gisements éocènes. Bulletin Du BRGM 2, 7–18.

Hausegger, S., Kurz, W., Rabitsch, R., Kiechl, E., Brosch, F.-J., 2010. Analysis of the internal structure of a carbonate damage zone: Implications for the mechanisms of fault breccia formation and fluid flow. Faulting and Fracturing of Carbonate Rocks: New Insights into Deformation Mechanisms, Petrophysics and Fluid Flow Properties 32, 1349–1362. https://doi.org/10.1016/j.jsg.2009.04.014

Heuberger, S., Célérier, B., Burg, J.-P., Chaudhry, N.M., Dawood, H., Hussain, S., 2010. Paleostress regimes from brittle structures of the Karakoram–Kohistan Suture Zone and surrounding areas of NW Pakistan. Journal of Asian Earth Sciences 38, 307–335. https://doi.org/10.1016/j.jseaes.2010.01.004

Hibsch, C., Cartwright, J., Hansen, D.M., Gaviglio, P., André, G., Cushing, M., Bracq, P., Juignet, P., Benoit, P., Allouc, J., 2003. Normal faulting in chalk: tectonic stresses vs. compaction-related polygonal faulting. Geological Society, London, Special Publications 216, 291. https://doi.org/10.1144/GSL.SP.2003.216.01.19

Kaminskaite, I., Fisher, Q.J., Michie, E.A.H., 2019. Microstructure and petrophysical properties of deformation bands in high porosity carbonates. Journal of Structural Geology 119, 61–80. https://doi.org/10.1016/j.jsg.2018.12.001

Kelly, P.G., Sanderson, D.J., Peacock, D.C.P., 1998. Linkage and evolution of conjugate strike-slip fault zones in limestones of Somerset and Northumbria. Journal of Structural Geology 20, 1477–1493. https://doi.org/10.1016/S0191-8141(98)00048-0

Laronne Ben-Itzhak, L., Aharonov, E., Karcz, Z., Kaduri, M., Toussaint, R., 2014. Sedimentary stylolite networks and connectivity in limestone: Large-scale field observations and implications for structure evolution. Journal of Structural Geology 63, 106–123. https://doi.org/10.1016/j.jsg.2014.02.010

Lin, S., Jiang, D., Williams, P.F., 2007. Importance of differentiating ductile slickenside striations from stretching lineations and variation of shear direction across a high-strain zone. Journal of Structural Geology 29, 850–862. https://doi.org/10.1016/j.jsg.2006.12.006

Lin, S., Williams, P.F., 1992. The origin of ridge-in-groove slickenside striae and associated steps in an S-C mylonite. Journal of Structural Geology 14, 315–321. https://doi.org/10.1016/0191-8141(92)90089-F

Maerten, L., Seranne, M., 1995. Extensional tectonics of the Oligo-Miocene Herault Basin (S. France), Gulf of Lion margin. Bulletin de La Société Géologique de France 166, 739–749.

Marshak, S., Geiser, P.A., Alvarez, W., Engelder, T., 1982. Mesoscopic fault array of the northern Umbrian Apennine fold belt, Italy: Geometry of conjugate shear by pressure-solution slip. GSA Bulletin 93, 1013–1022. https://doi.org/10.1130/0016-7606(1982)93<1013:MFAOTN>2.0.CO;2

753 Mayolle, S., Soliva, R., Caniven, Y., Wibberley, C., Ballas, G., Milesi, G., Dominguez, S., 2019. Scaling of
754 fault damage zones in carbonate rocks. Journal of Structural Geology 124, 35–50.
755 https://doi.org/10.1016/j.jsg.2019.03.007
756 Mazzoli, S., Di Bucci, D., 2003. Critical displacement for normal fault nucleation from en-échelon vein
757 arrays in limestones: a case study from the southern Apennines (Italy). Journal of Structural
758 Geology 25, 1011–1020. https://doi.org/10.1016/S0191-8141(02)00156-6
759 Means, W.D., 1987. A newly recognized type of slickenside striation. Journal of Structural Geology 9,
760 585–590. https://doi.org/10.1016/0191-8141(87)90143-X
761 Meng, Q., Hao, F., Tian, J., 2021. Origins of non-tectonic fractures in shale. Earth-Science Reviews 222,
762 103825. https://doi.org/10.1016/j.earscirev.2021.103825
763 Micarelli, L., Benedicto, A., 2008. Normal fault terminations in limestones from the SE-Basin (France):
764 implications for fluid flow. Geological Society, London, Special Publications 299, 123.
765 https://doi.org/10.1144/SP299.8
766 Micarelli, L., Benedicto, A., Wibberley, C.A.J., 2006. Structural evolution and permeability of normal fault
767 zones in highly porous carbonate rocks. Journal of Structural Geology 28, 1214–1227.
768 https://doi.org/10.1016/j.jsg.2006.03.036
769 Milliken, K.L., Reed, R.M., 2010. Multiple causes of diagenetic fabric anisotropy in weakly consolidated
770 mud, Nankai accretionary prism, IODP Expedition 316. Structural Diagenesis 32, 1887–1898.
771 https://doi.org/10.1016/j.jsg.2010.03.008
772 Mitchell, J.K., Soga, K., 2005. Fundamentals of soil behavior, John Wiley and Sons. ed.
773 Mollema, P.N., Antonellini, M.A., 1996. Compaction bands: a structural analog for anti-mode I cracks in
774 aeolian sandstone. Tectonophysics 267, 209–228. https://doi.org/10.1016/S0040-
775 1951(96)00098-4
776 Morris, A.P., Ferrill, D.A., 2009. The importance of the effective intermediate principal stress (σ'2) to fault
777 slip patterns. Journal of Structural Geology 31, 950–959.
778 https://doi.org/10.1016/j.jsg.2008.03.013
779 Peacock, D.C.P., Sanderson, D.J., 1995. Pull-aparts, shear fractures and pressure solution. Tectonophysics
780 241, 1–13. https://doi.org/10.1016/0040-1951(94)00184-B
781 Petit, J.-P., Laville, E., 1987. Morphology and microstructures of hydroplastic slickensides in sandstone.
782 Geological Society, London, Special Publications 29, 107.
783 https://doi.org/10.1144/GSL.SP.1987.029.01.10
784 Petit, J.-P., Mattauer, M., 1995. Palaeostress superimposition deduced from mesoscale structures in
785 limestone: the Matelles exposure, Languedoc, France. Journal of Structural Geology 17, 245–256.
786 https://doi.org/10.1016/0191-8141(94)E0039-2
787 Philit, S., Soliva, R., Castilla, R., Ballas, G., Taillefer, A., 2018. Clusters of cataclastic deformation bands in
788 porous sandstones. Journal of Structural Geology 114, 235–250.
789 https://doi.org/10.1016/j.jsg.2018.04.013
790 Philit, S., Soliva, R., Labaume, P., Gout, C., Wibberley, C., 2015. Relations between shallow cataclastic
791 faulting and cementation in porous sandstones: First insight from a groundwater environmental
792 context. Journal of Structural Geology 81, 89–105. https://doi.org/10.1016/j.jsg.2015.10.001
793 Risnes, R., 2001. Deformation and yield in high porosity outcrop chalk. Physics and Chemistry of the
794 Earth, Part A: Solid Earth and Geodesy 26, 53–57. https://doi.org/10.1016/S1464-
795 1895(01)00022-9
796 Risnes, R., Madland, M.V., Hole, M., Kwabiah, N.K., 2005. Water weakening of chalk— Mechanical effects
797 of water–glycol mixtures. Journal of Petroleum Science and Engineering 48, 21–36.
798 https://doi.org/10.1016/j.petrol.2005.04.004
799 Rispoli, R., 1981. Stress fields about strike-slip faults inferred from stylolites and tension gashes.
800 Tectonophysics 75, T29–T36. https://doi.org/10.1016/0040-1951(81)90274-2

Robert, R., Robion, P., Souloumiac, P., David, C., Saillet, E., 2018. Deformation bands, early markers of tectonic activity in front of a fold-and-thrust belt: Example from the Tremp-Graus basin, southern Pyrenees, Spain. Journal of Structural Geology 110, 65–85. https://doi.org/10.1016/j.jsg.2018.02.012

Roche, V., Homberg, C., Rocher, M., 2012. Architecture and growth of normal fault zones in multilayer systems: A 3D field analysis in the South-Eastern Basin, France. Journal of Structural Geology 37, 19–35. https://doi.org/10.1016/j.jsg.2012.02.005

Rotevatn, A., Thorsheim, E., Bastesen, E., Fossmark, H.S.S., Torabi, A., Sælen, G., 2016. Sequential growth of deformation bands in carbonate grainstones in the hangingwall of an active growth fault: Implications for deformation mechanisms in different tectonic regimes. Journal of Structural Geology 90, 27–47. https://doi.org/10.1016/j.jsg.2016.07.003

Rotevatn, A., Torabi, A., Fossen, H., Braathen, A., 2008. Slipped deformation bands: A new type of cataclastic deformation bands in Western Sinai, Suez rift, Egypt. Journal of Structural Geology 30, 1317–1331. https://doi.org/10.1016/j.jsg.2008.06.010

Rustichelli, A., Tondi, E., Agosta, F., Cilona, A., Giorgioni, M., 2012. Development and distribution of bed-parallel compaction bands and pressure solution seams in carbonates (Bolognano Formation, Majella Mountain, Italy). Journal of Structural Geology 37, 181–199. https://doi.org/10.1016/j.jsg.2012.01.007

Saillet, E., Wibberley, C.A.J., 2013. Permeability and flow impact of faults and deformation bands in high-porosity sand reservoirs: Southeast Basin, France, analog. AAPG Bulletin 97, 437–464. https://doi.org/10.1306/09071211191

Saillet, E., Wibberley, C.A.J., 2010. Evolution of cataclastic faulting in high-porosity sandstone, Bassin du Sud-Est, Provence, France. Fault Zones 32, 1590–1608. https://doi.org/10.1016/j.jsg.2010.02.007

Schröckenfuchs, T., Bauer, H., Grasemann, B., Decker, K., 2015. Rock pulverization and localization of a strike-slip fault zone in dolomite rocks (Salzach–Ennstal–Mariazell–Puchberg fault, Austria). Journal of Structural Geology 78, 67–85. https://doi.org/10.1016/j.jsg.2015.06.009

Schultz, R.A., Fossen, H., 2002. Displacement–length scaling in three dimensions: the importance of aspect ratio and application to deformation bands. Journal of Structural Geology 24, 1389–1411. https://doi.org/10.1016/S0191-8141(01)00146-8

Schultz, R.A., Siddharthan, R., 2005. A general framework for the occurrence and faulting of deformation bands in porous granular rocks. Tectonophysics 411, 1–18. https://doi.org/10.1016/j.tecto.2005.07.008

Séranne, M., Camus, H., Lucazeau, F., Barbarand, J., Quinif, Y., 2002. Polyphased uplift and erosion of the Cévennes (southern France). An example of slow morphogenesis. Bulletin de La Société Géologique de France 173, 97–112. https://doi.org/10.2113/173.2.97

Shipton, Z.K., Cowie, P.A., 2003. A conceptual model for the origin of fault damage zone structures in high-porosity sandstone. Journal of Structural Geology 25, 333–344. https://doi.org/10.1016/S0191-8141(02)00037-8

Smith, S.A.F., Di Toro, G., Kim, S., Ree, J.-H., Nielsen, S., Billi, A., Spiess, R., 2013. Coseismic recrystallization during shallow earthquake slip. Geology 41, 63–66. https://doi.org/10.1130/G33588.1

Soliva, R., Benedicto, A., 2004. A linkage criterion for segmented normal faults. Journal of Structural Geology 26, 2251–2267. https://doi.org/10.1016/j.jsg.2004.06.008

Soliva, R., Philit, S., Ballas, G., Fossen, H., 2016. Tectonic regime controls clustering of deformation bands in porous sandstone. Geology 44, 423–426. https://doi.org/10.1130/G37585.1

Soliva, R., Schultz, R.A., Ballas, G., Taboada, A., Wibberley, C., Saillet, E., Benedicto, A., 2013. A model of strain localization in porous sandstone as a function of tectonic setting, burial and material

properties; new insight from Provence (southern France). Journal of Structural Geology 49, 50–63. https://doi.org/10.1016/j.jsg.2012.11.011
Solum, J.G., Brandenburg, J.P., Naruk, S.J., Kostenko, O.V., Wilkins, S.J., Schultz, R.A., 2010. Characterization of deformation bands associated with normal and reverse stress states in the Navajo Sandstone, Utah. AAPG Bulletin 94, 1453–1475. https://doi.org/10.1306/01051009137
Tajima, F., Célérier, B., 1989. Possible focal mechanism change during reactivation of a previously ruptured subduction zone and stress tensor implications. Geophysical Journal International 98, 301–316. https://doi.org/10.1111/j.1365-246X.1989.tb03354.x
Tavani, S., Granado, P., Balsamo, F., Pizzati, M., Cantarero, I., Corradetti, A., Muñoz, J.A., 2018a. Shear-enhanced compaction-solution bands in quartz-rich calcarenites of the Cotiella Massif (Spanish Pyrenees). Journal of Structural Geology 114, 274–279. https://doi.org/10.1016/j.jsg.2017.11.018
Tavani, S., Granado, P., Balsamo, F., Pizzati, M., Cantarero, I., Corradetti, A., Muñoz, J.A., 2018b. Shear-enhanced compaction-solution bands in quartz-rich calcarenites of the Cotiella Massif (Spanish Pyrenees). Journal of Structural Geology 114, 274–279. https://doi.org/10.1016/j.jsg.2017.11.018
Tewksbury, B.J., Hogan, J.P., Kattenhorn, S.A., Mehrtens, C.J., Tarabees, E.A., 2014. Polygonal faults in chalk: Insights from extensive exposures of the Khoman Formation, Western Desert, Egypt. Geology 42, 479–482. https://doi.org/10.1130/G35362.1
Tondi, E., Antonellini, M., Aydin, A., Marchegiani, L., Cello, G., 2006. The role of deformation bands, stylolites and sheared stylolites in fault development in carbonate grainstones of Majella Mountain, Italy. Journal of Structural Geology 28, 376–391. https://doi.org/10.1016/j.jsg.2005.12.001
Toussaint, R., Aharonov, E., Koehn, D., Gratier, J.-P., Ebner, M., Baud, P., Rolland, A., Renard, F., 2018. Stylolites: A review. Journal of Structural Geology 114, 163–195. https://doi.org/10.1016/j.jsg.2018.05.003
Tueckmantel, C., Fisher, Q.J., Knipe, R.J., Lickorish, H., Khalil, S.M., 2010. Fault seal prediction of seismic-scale normal faults in porous sandstone: A case study from the eastern Gulf of Suez rift, Egypt. Marine and Petroleum Geology 27, 334–350. https://doi.org/10.1016/j.marpetgeo.2009.10.008
Ujiie, K., Maltman, A.J., Sánchez-Gómez, M., 2004. Origin of deformation bands in argillaceous sediments at the toe of the Nankai accretionary prism, southwest Japan. Journal of Structural Geology 26, 221–231. https://doi.org/10.1016/j.jsg.2003.06.001
Vajdova, V., Baud, P., Wong, T., 2004. Compaction, dilatancy, and failure in porous carbonate rocks. Journal of Geophysical Research: Solid Earth 109. https://doi.org/10.1029/2003JB002508
Wallace, R.E., 1951. Geometry of Shearing Stress and Relation to Faulting. The Journal of Geology 59, 118–130. https://doi.org/10.1086/625831
Wennberg, O.P., Casini, G., Jahanpanah, A., Lapponi, F., Ineson, J., Wall, B.G., Gillespie, P., 2013. Deformation bands in chalk, examples from the Shetland Group of the Oseberg Field, North Sea, Norway. Journal of Structural Geology 56, 103–117. https://doi.org/10.1016/j.jsg.2013.09.005
Wibberley, C.A.J., Petit, J.-P., Rives, T., 2007. The mechanics of fault distribution and localization in high-porosity sands, Provence, France. Geological Society, London, Special Publications 289, 19. https://doi.org/10.1144/SP289.3
Will, T.M., Wilson, C.J.L., 1989. Experimentally produced slickenside lineations in pyrophyllitic clay. Journal of Structural Geology 11, 657–667. https://doi.org/10.1016/0191-8141(89)90002-3
Willemse, E.J.M., Peacock, D.C.P., Aydin, A., 1997. Nucleation and growth of strike-slip faults in limestones from Somerset, U.K. Journal of Structural Geology 19, 1461–1477. https://doi.org/10.1016/S0191-8141(97)00056-4

Wong, T., Baud, P., 2012. The brittle-ductile transition in porous rock: A review. Journal of Structural Geology 44, 25–53. https://doi.org/10.1016/j.jsg.2012.07.010

Caption List

Fig. 1. (a) Schematic geological map of the study area modified from the 1/1 000 000 geological map of France. **(b)** SSW- NE Structural cross-section within the Aumelas - La Boissière basin using field cartographic measurements and the St Bauzille Well data. La Taillade is the study site.

Fig. 2. (a) Aerial pictures (GoogleEarth) showing the location of the studied outcrop along the A750 highway. The reported geological map is modified form the 1/50 000 maps of Montpellier (Bonnet et al., 1971) and Lodève (Alabouvette et al., 1982). Main bed dip values are reported for the three main parts of the outcrop. The main studied section is located westward. A second studied outcrop is located eastward but is potentially disconnected form the other studied exposures by map-scale sinistral faults. **(b)** Field view of the main studied limestone-dominated section. **(c)** Details of the studied outcrop showing mudstone beds. **(d)** Example of brownish silty marl deposits intercalated in mudstone beds.

Fig. 3. Host rock microstructure observed from SEM images. **(a)** 3D mudstone sample showing micritic euhedral crystals of calcite less than 5 μm in size. **(b)** Image from thin-section showing imbricated contact between calcite particles.

Fig. 4. Sedimentological log of the main studied section showing location of studied faults along the succession. Evidence of pedogenetic alterations (desiccation, karstification, brecciation) observed on bed surfaces are also reported. Beds are draw following the Dunham classification (*M*: Mudstone, *W*: Wackstone, *P*: Packestone, *G*: Grainstone, *B*: Boundstone + *C* to identify clays). Studied fault symbol represents indifferently both normal-sense and strike-slip fault sets.

Fig. 5. Slickenside morphology. **(a)** example of slickenside from a normal-sense fault. **(b), (c), and (d)** Detailed observations of grooves and ridges morphology and tips. **(e)** SEM image showing slickenlines morphology at the microscale. **(f)** SEM image showing the 3D morphology of a step marking on a slickenside. Thick arrows show the sense of displacement of the absent wall.

Fig. 6. Normal fault system. **(a)** Limestone layers containing constrained normal-sense faults. **(b)** and **(c)** S-Shape of faults**. (d)** and **(e)** Cross-section of limestone beds showing the conjugate system of faults**.** White arrows show the fault kinematic. *S0* is the bedding (base of the succession at the bottom of the photography).

Fig. 7. Stereographic analysis of normal-sense fault set. **(a)** Stereograms showing projection of fault planes and slickenlines. **(b)** Histogram of fault dip. **(c)** Histogram of fault rake. (Restored data)

Fig. 8. Strike-slip fault system. **(a)** and **(b)** Examples of dextral and sinistral fault slickensides, respectively. **(c)** Bed surface showing the conjugate sets of strike-slip faults. **(d)** Detailed view of dilation jogs showing the fault kinematic and the centimeter-scale shear-displacement. White arrows show the fault kinematic.

938 **Fig. 9.** Stereographic analysis of strike-slip fault set. **(a)** Stereograms showing projection of fault
939 planes and slickenlines (grooves). **(b)** Histogram of fault dip. **(c)** Histogram of fault rake.
940 (Restored data)

941 **Fig. 10.** Interaction between both conjugate fault sets. **(a)** and **(b)** Continuity between normal-
942 sense and strike-slip faults**. (c)** Schematic bloc diagram showing faults organization. **(d)**
943 Photograph showing the pervasive distribution of both normal-sense and strike-slip fault systems.
944 White and red arrows show the fault kinematic. *S0* is the bedding (base of the succession at the
945 bottom of the photography). See the evidence of shear offset of the NNW-SSE trending sinistral
946 fault fig. 10a.

947 **Fig. 11.** Microstructure of faults. **(a)** Mosaic of SEM images showing the rock microstructure
948 below the fault slickensides and photograph of the block sample (see the orientation and dip of
949 the fault). **(b)** Focus on the compacted zone above the main fault plane. **(c)** Example of the
950 compressive jog showing compaction and evidences of enhanced pressure-solution. **(d)** Other
951 example of the compacted zone below the fault plane. **(e)** Example of fault step marking at the
952 upper tip of groove. This example illustrates the presence of dilation joint and the lack of
953 compaction.

954 **Fig. 12.** Grain framework reconstruction maps form EBSD acquisition and rose diagram of grain
955 slope (angle from the image top) in **(a)** the host rock, **(b)** and **(c)** the compressive jogs along the
956 fault plane. The color of grain indicates the angle of their crystallographic preferred orientation
957 with the different calcite crystallographic axis (*0001*: c-axis; *0110* and *1010*: a-axes).

958 **Fig. 13.** Crystallographic preferred orientation (CPO) in the fault zone, EBSD acquisitions. **(a)**
959 Grain framework reconstruction maps from EBSD acquisition showing deformation zone above

960 the main fault surface. **(b)** Calcite orientation data for grains of the fault zone (within dashed line
961 in (a)). (*0001*: c-axis; *0110, 1010* and *1120*: a-axes).

962 **Fig. 14. (a)** EBSD acquisitions showing example of calcite twinning within the fault core. Maps
963 of calcite twins detected at the fault core **(b)**, a compressive jog **(c)**, and a step marking **(d)**. The
964 calcite twins are draw by red lines. High concentration of calcite twins is observed in the fault
965 core and along the compressive jog whereas no twins are observed in the host rocke and at
966 marking dilatant step.

967 **Fig. 15.** Stress state during fault formation. **(a)** Stereogram projection showing state of stress
968 determination by inversion method. (r_0: stress tensor aspect ratio; s_1, s_2, s_3, principal stress
969 orientations). **(b)** Table showing stress inversion parameters. **(c)** Reduced Mohr circle. The faults
970 are color coded as a function of their angular misfit range: 0-5° blue, 5-15° magenta, 15-30°
971 green, 30-180° grey. The procedure is detailed in Appendix 1 of Burg *et al.* (1995). *Ntotal*: Total
972 number of fault slip data. *Pinv*: Proportion of slip data used in the inversion. $\Delta\lambda_{cav}$: Average
973 angular misfit of the rake; this average is computed on the *Pinv* lowest misfits only (Etchecopar
974 *et al.*, 1981). N_{exp15}: Number of fault slip data with rake misfit < 15°. $N0_{exp15:}$ Number of fault slip
975 data with rake misfit < 15° that could be obtained from a random sample. *InvQual*: Quality index
976 as in Heuberger *et al.* (2010).

977 **Fig. 16.** Multi-beds normal faults. **(a)** Exposure of such fault. **(b)** Detail of slickenside
978 morphology showing slickolites (teeth evidencing pressure-solution at the down-slip ends of
979 grooves). **(c)** Stereographic data showing faults organization (bedding restored to horizontal). **(d)**
980 Example of such faults with their estimated shear-displacement. White arrows show the fault
981 kinematic. *S0* is the bedding. *ds* is the apparent shear displacement.

Fig. 17. Conceptual model of faults formation. **(a)** Differential Stress (Q) – Mean Effective Stress (P) space diagram showing location of faults formation using yield envelops of porous carbonates (Risnes *et al.* 2005) and estimated stress path *(Ko* : coefficient of Earth Pressure at Rest; blue lines: estimated stress paths). **(b)** The successive stages of faults formation: comminuted zone with dynamic recrystallization (stage 1), shear localization (stage 2), and early blocking of fault movement by grain rotation and pressure-solution processes (stage 3). **(c)** 3D schematic bloc diagram showing the location of fault in the basin and the influence of the slope.

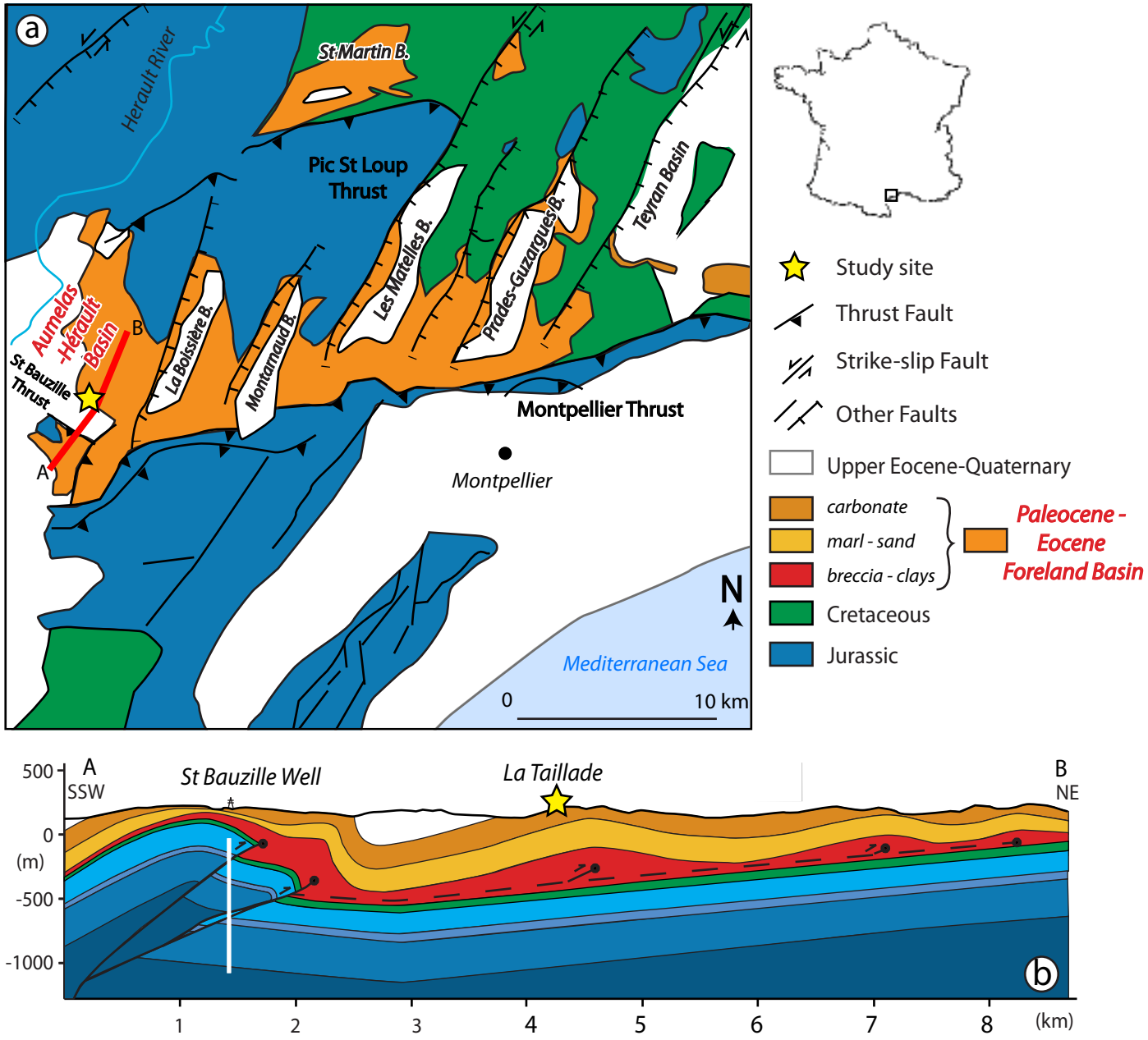
a
Herault River
St Martin B.
Pic St Loup Thrust
Les Matelles B.
Prades-Guzargues B.
Teyran Basin
Aumelas -Hérault Basin
St Bauzille Thrust
La Boissière B.
Montarnaud B.
Montpellier Thrust
Montpellier
A
B
N
Mediterranean Sea
0
10 km
Study site
Thrust Fault
Strike-slip Fault
Other Faults
Upper Eocene-Quaternary
carbonate
marl - sand
breccia - clays
Paleocene - Eocene Foreland Basin
Cretaceous
Jurassic
500
0
(m)
-500
-1000
A
SSW
St Bauzille Well
La Taillade
B
NE
b
1
2
3
4
5
6
7
8
(km)

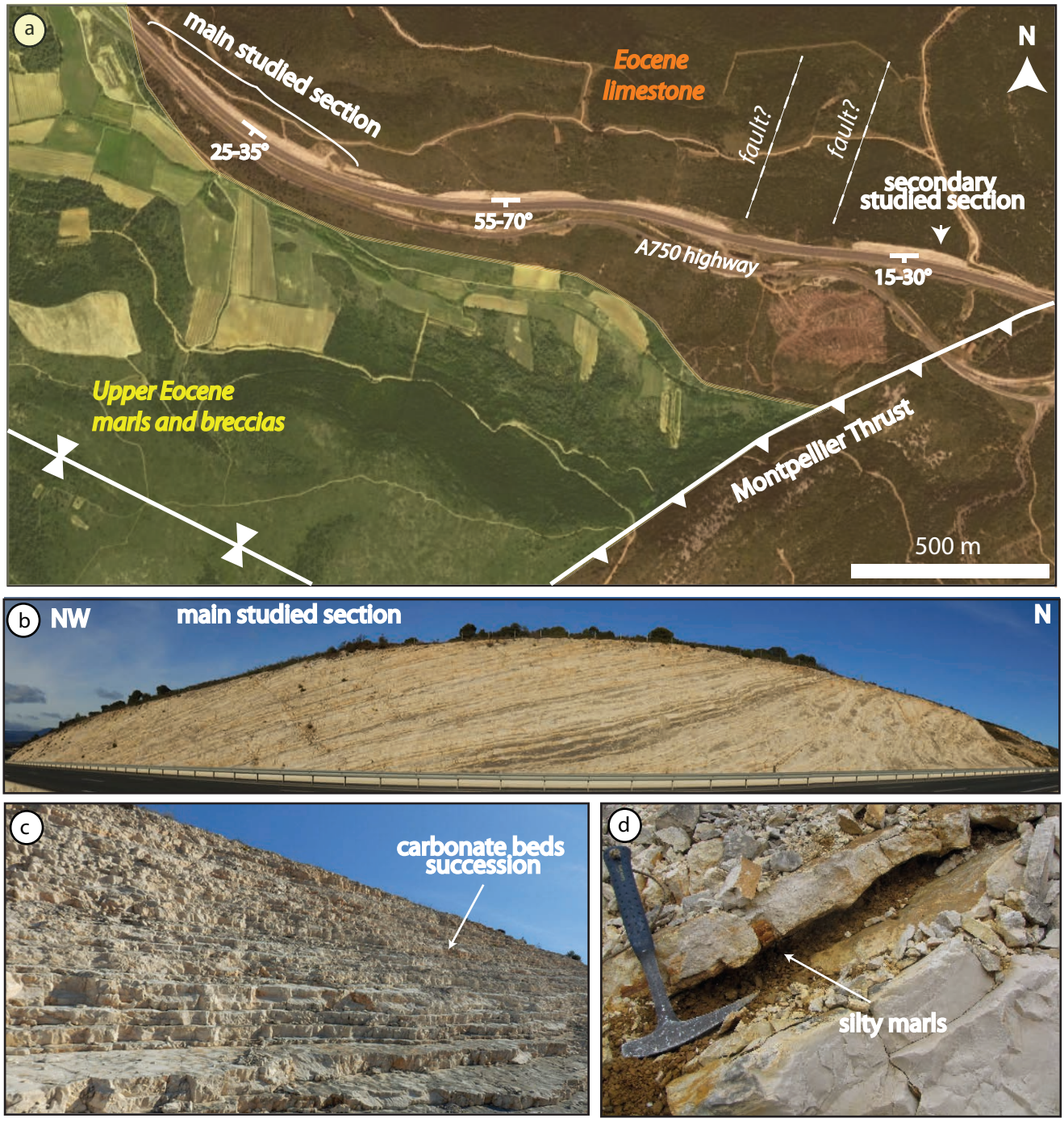
a
main studied section
25-35°
Eocene
limestone
fault?
fault?
N
secondary
studied section
55-70°
A750 highway
15-30°
Upper Eocene
marls and breccias
Montpellier Thrust
500 m
b
NW
main studied section
N
c
carbonate beds
succession
d
silty marls

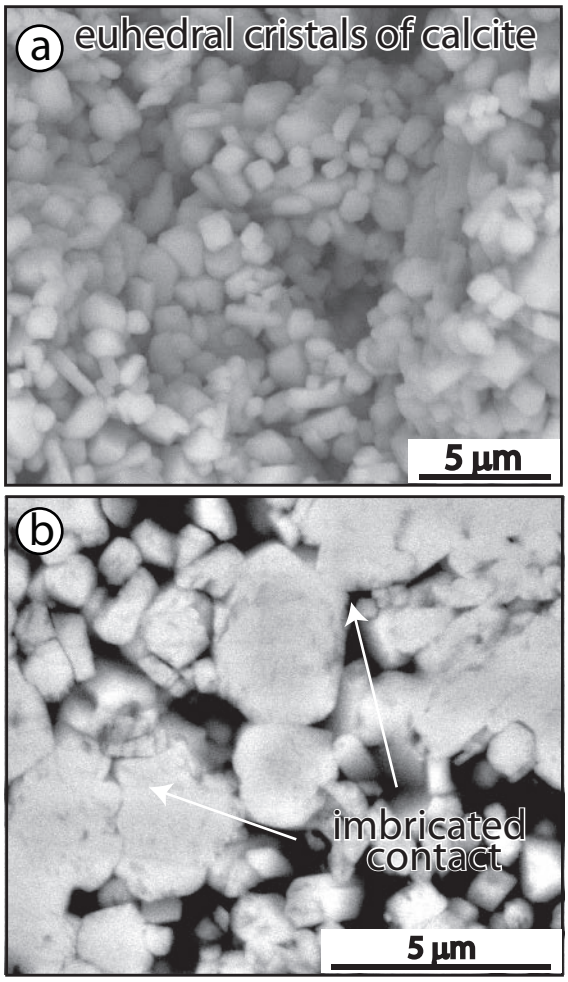
a
euhedral cristals of calcite
5 µm
b
imbricated
contact
5 µm

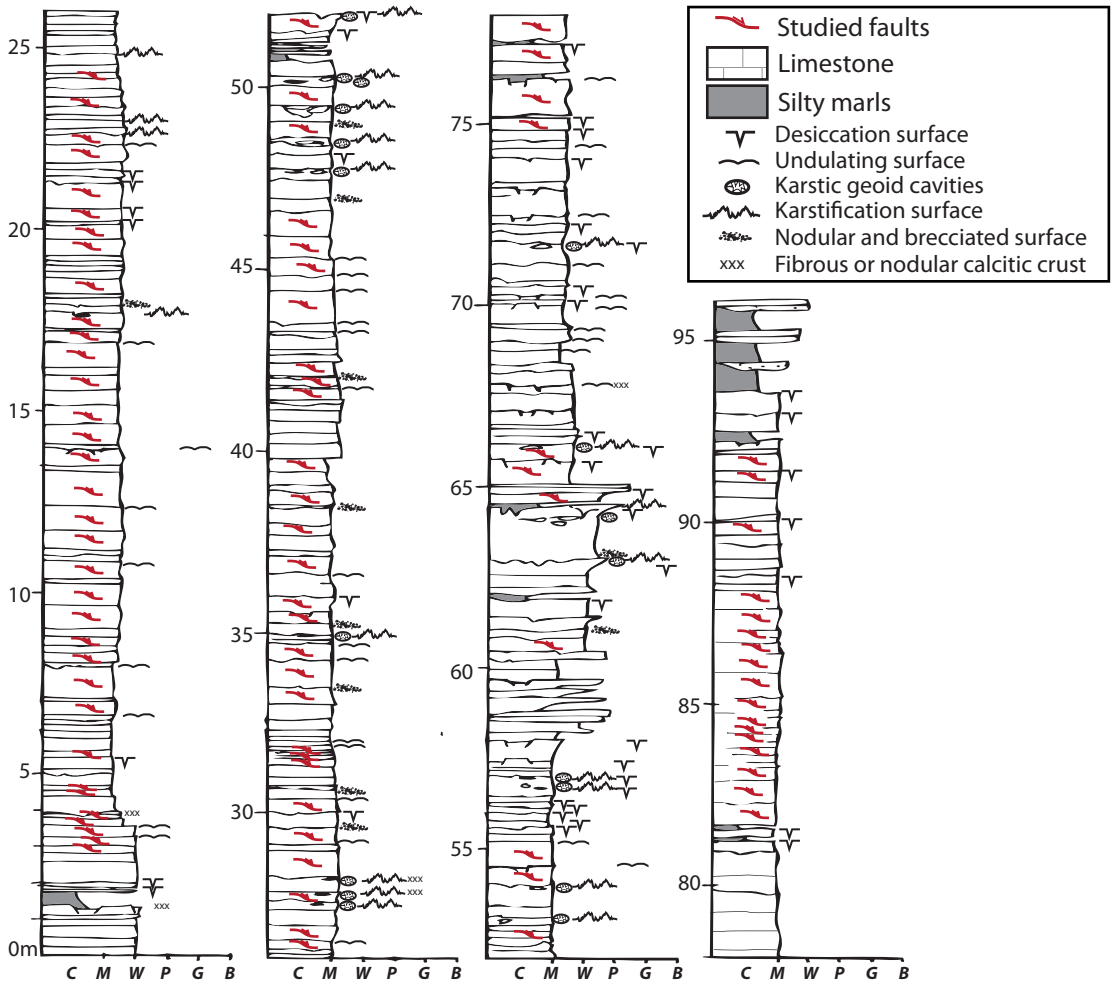
Studied faults
Limestone
Silty marls
Desiccation surface
Undulating surface
Karstic geoid cavities
Karstification surface
Nodular and brecciated surface
Fibrous or nodular calcitic crust
0m
5
10
15
20
25
30
35
40
45
50
55
60
65
70
75
80
85
90
95
C M W P G B

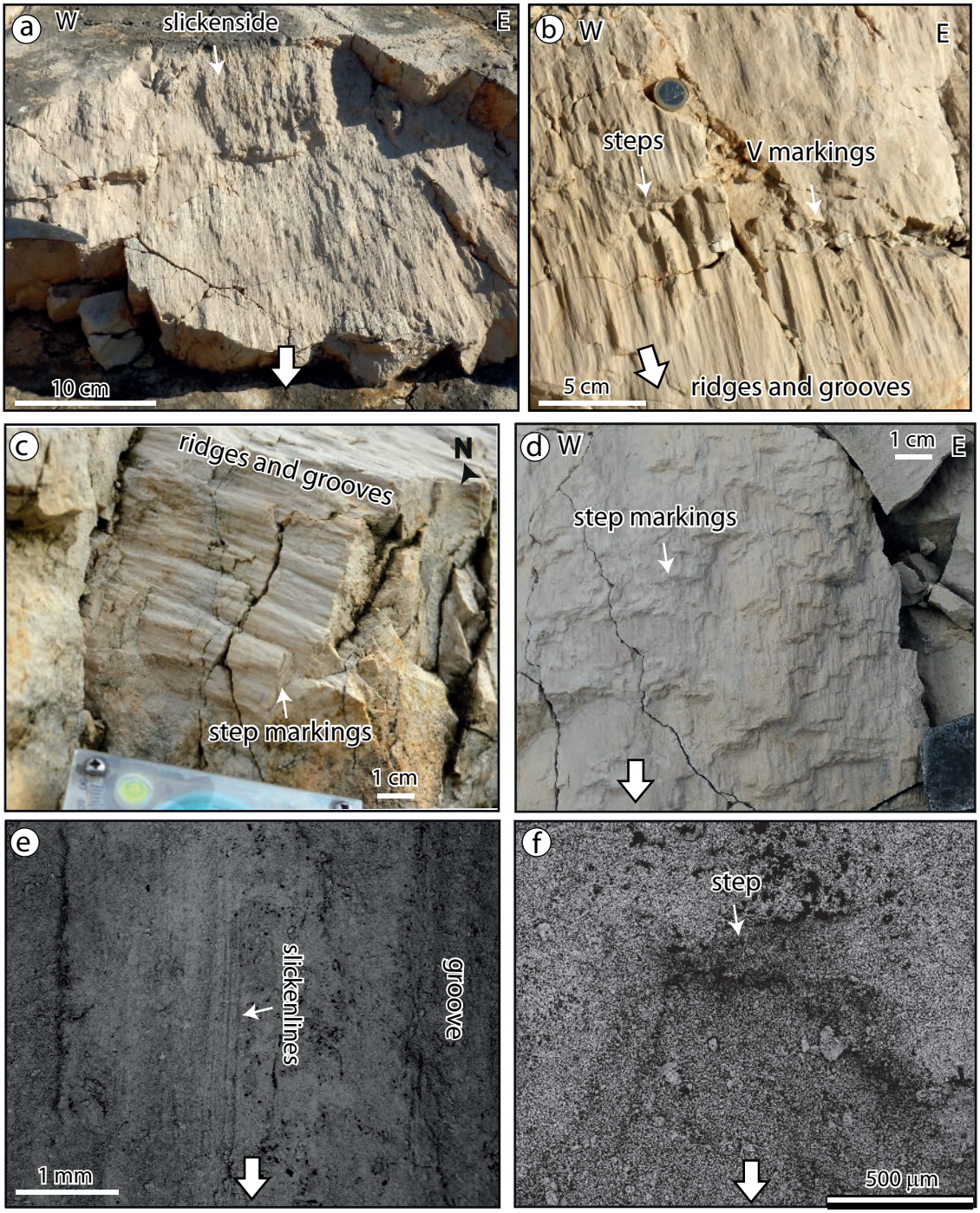
a
W
slickenside
E
10 cm
b
W
E
steps
V markings
5 cm
ridges and grooves
c
ridges and grooves
N
step markings
1 cm
d
W
1 cm
E
step markings
e
slickenlines
groove
1 mm
f
step
500 µm

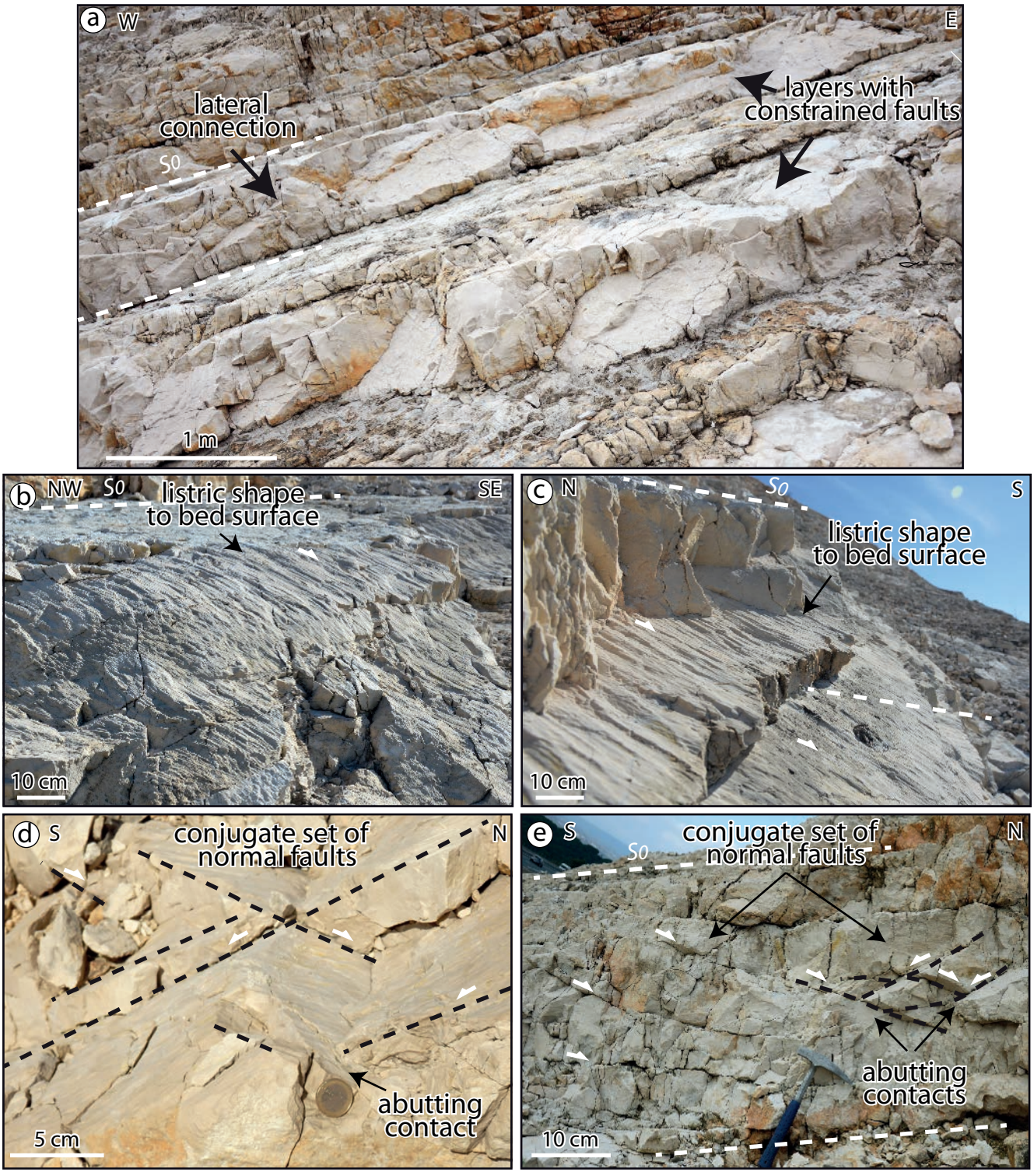
a
W
E
lateral
connection
S0
layers with
constrained faults
1 m
b
NW
S0
listric shape
to bed surface
SE
10 cm
c
N
S0
S
listric shape
to bed surface
10 cm
d
S
conjugate set of
normal faults
N
abutting
contact
5 cm
e
S
S0
conjugate set of
normal faults
N
abutting
contacts
10 cm

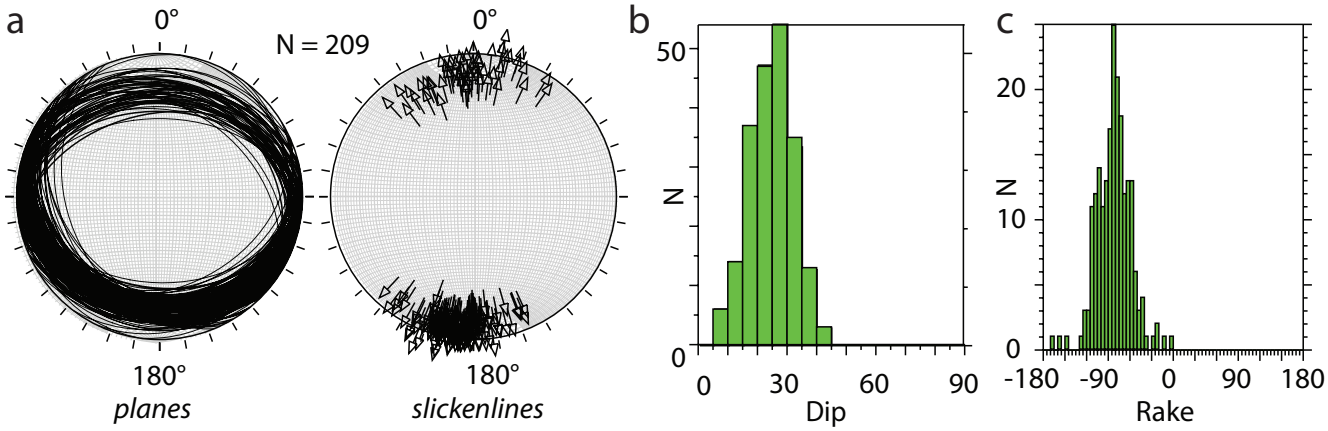
a
0°
N = 209
0°
180°
planes
180°
slickenlines
b
50
N
0
0
30
60
90
Dip
c
20
N
10
0
-180
-90
0
90
180
Rake

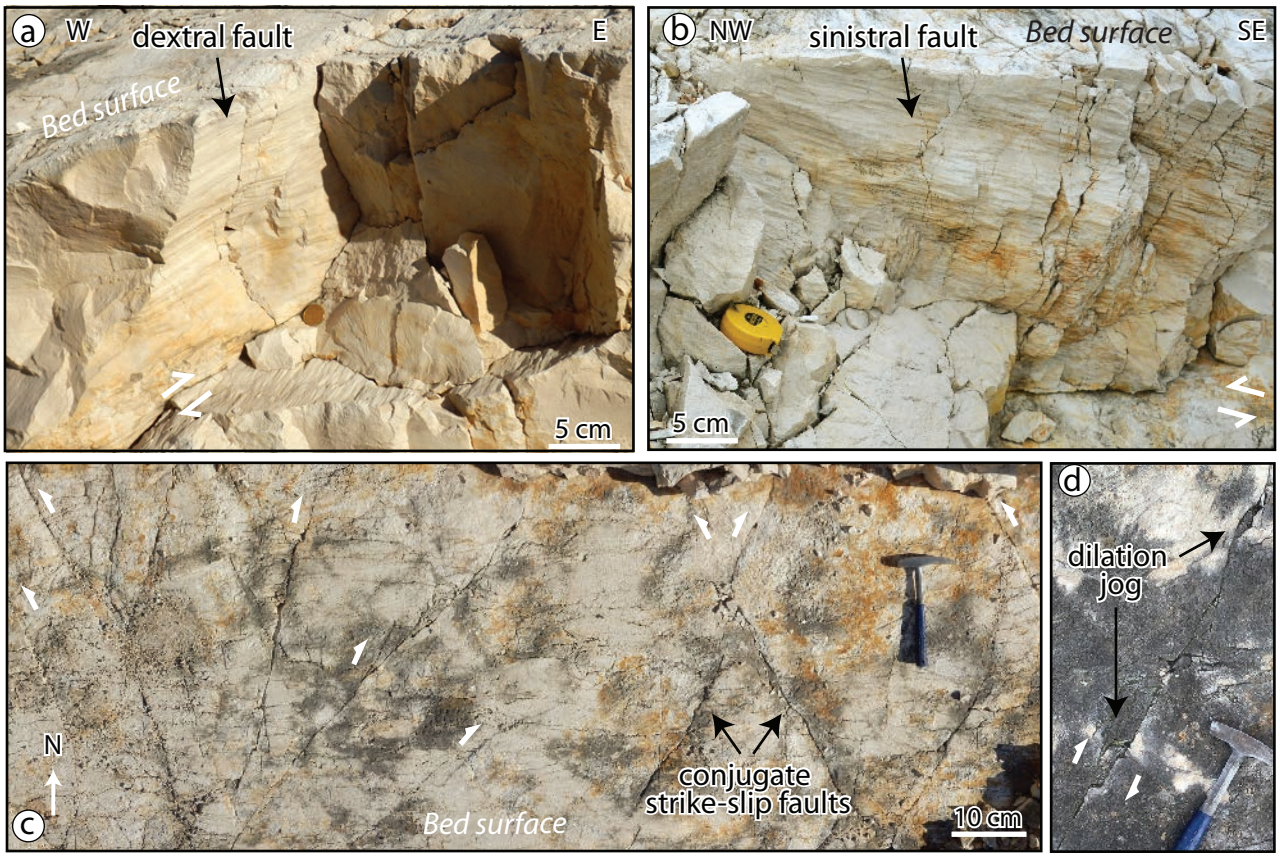
a
W
dextral fault
E
Bed surface
5 cm
b
NW
sinistral fault
Bed surface
SE
5 cm
c
N
conjugate
strike-slip faults
Bed surface
10 cm
d
dilation
jog

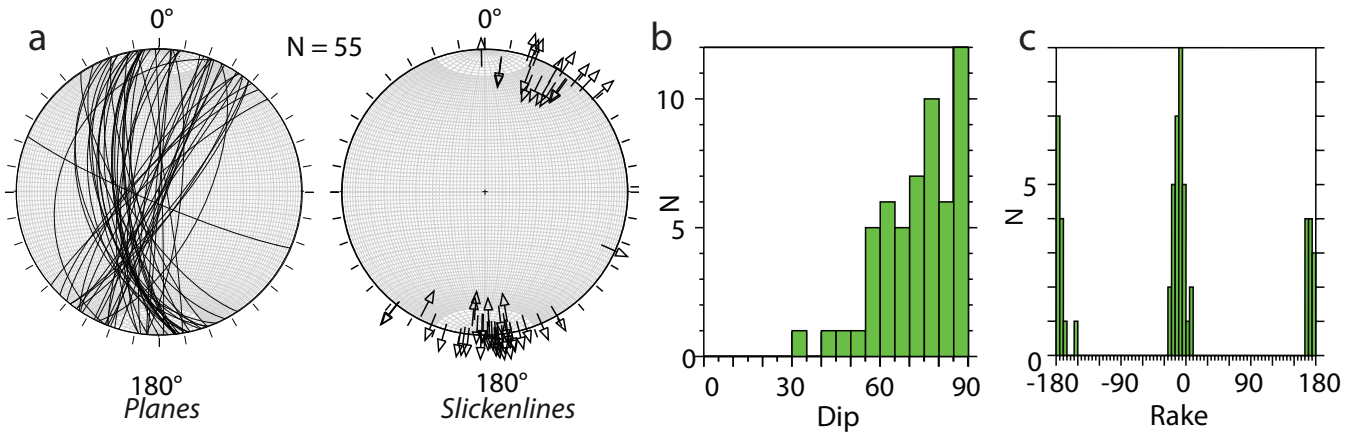
a
0°
N = 55
180°
Planes
0°
180°
Slickenlines
b
10
5
0
N
0
30
60
90
Dip
c
5
0
N
-180
-90
0
90
180
Rake

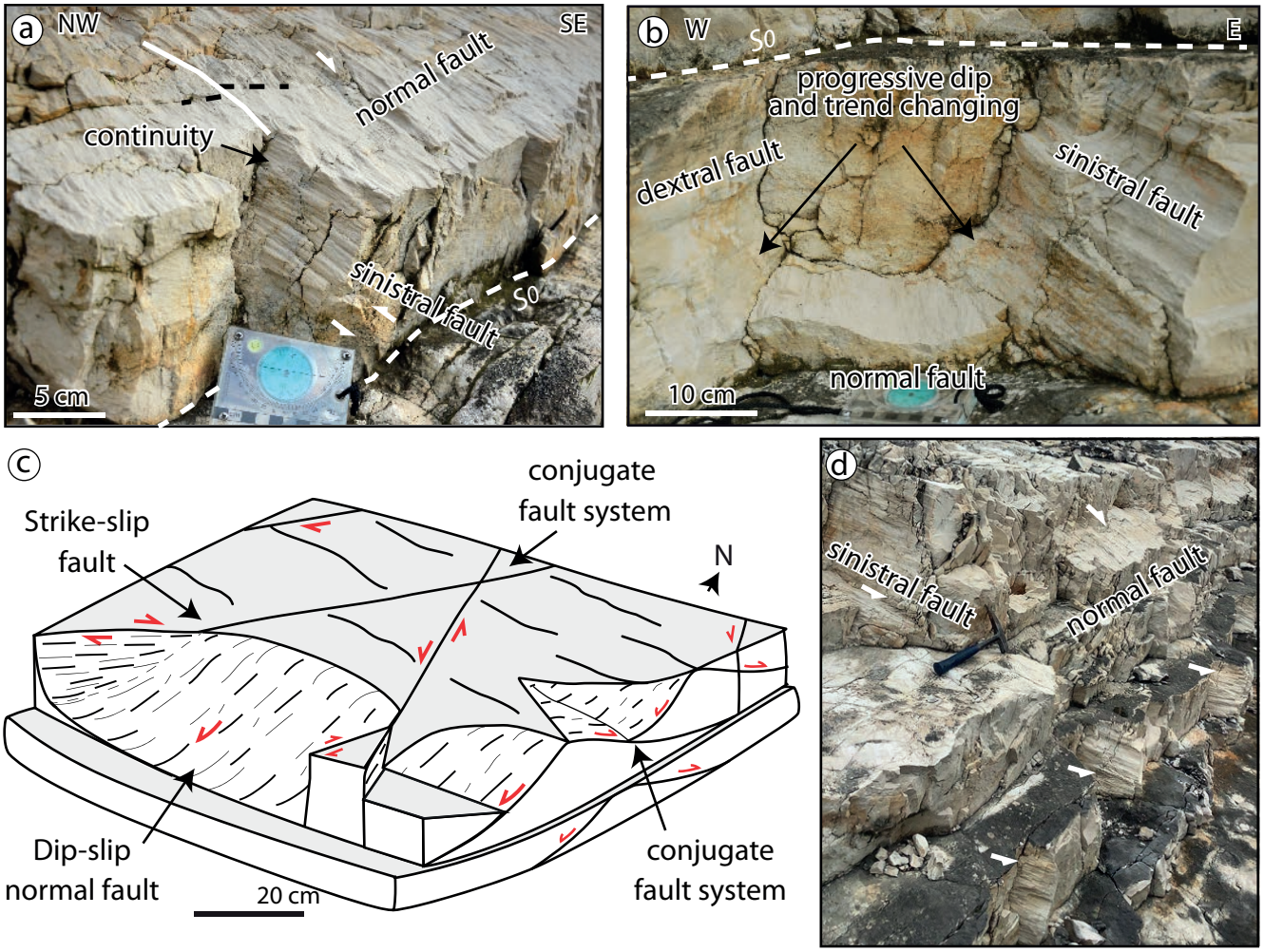
a
NW
SE
normal fault
continuity
sinistral fault
S0
5 cm
b
W
S0
E
progressive dip
and trend changing
dextral fault
sinistral fault
10 cm
normal fault
c
conjugate
fault system
Strike-slip
fault
N
Dip-slip
normal fault
20 cm
conjugate
fault system
d
sinistral fault
normal fault

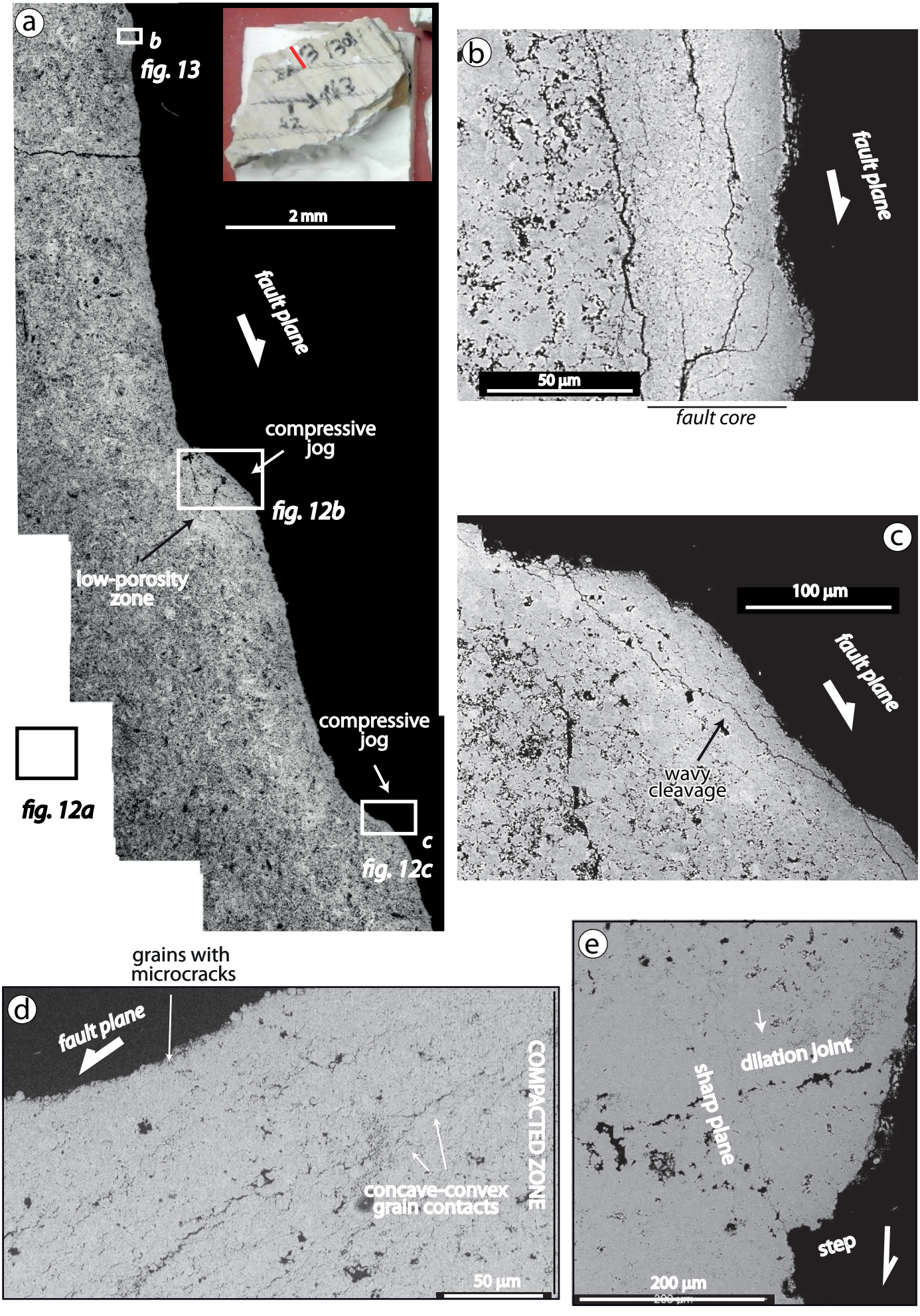
a
b
fig. 13
2 mm
fault plane
compressive jog
fig. 12b
low-porosity zone
compressive jog
c
fig. 12c
fig. 12a
b
fault plane
50 µm
fault core
c
100 µm
fault plane
wavy cleavage
grains with microcracks
d
fault plane
COMPACTED ZONE
concave-convex grain contacts
50 µm
e
dilation joint
sharp plane
step
200 µm

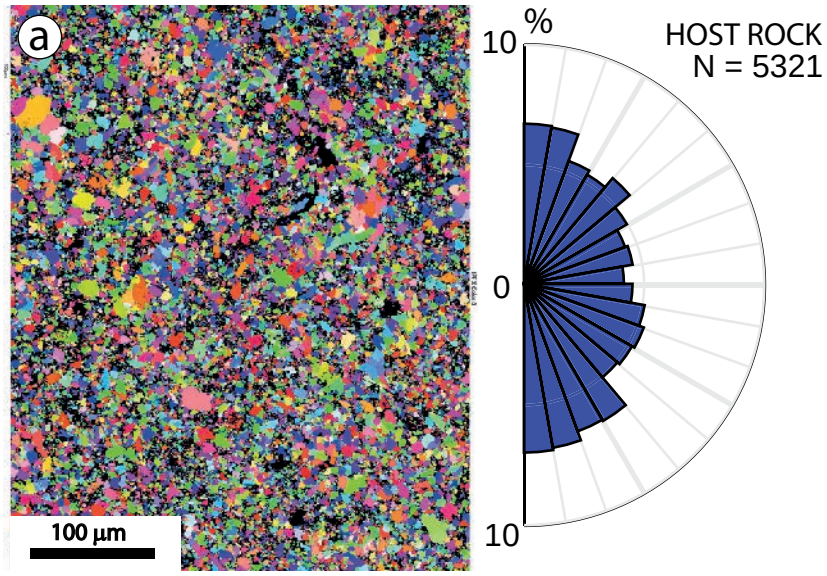
a
100 µm
%
10
0
10
HOST ROCK
N = 5321

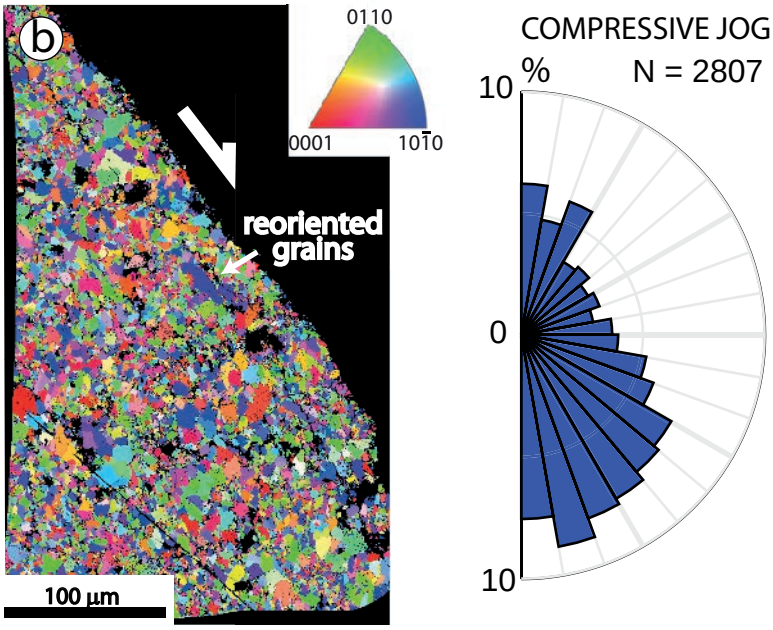
b
0110
0001
10$\bar{1}$0
reorientated
grains
100 µm
COMPRESSIVE JOG
N = 2807
%
10
0
10

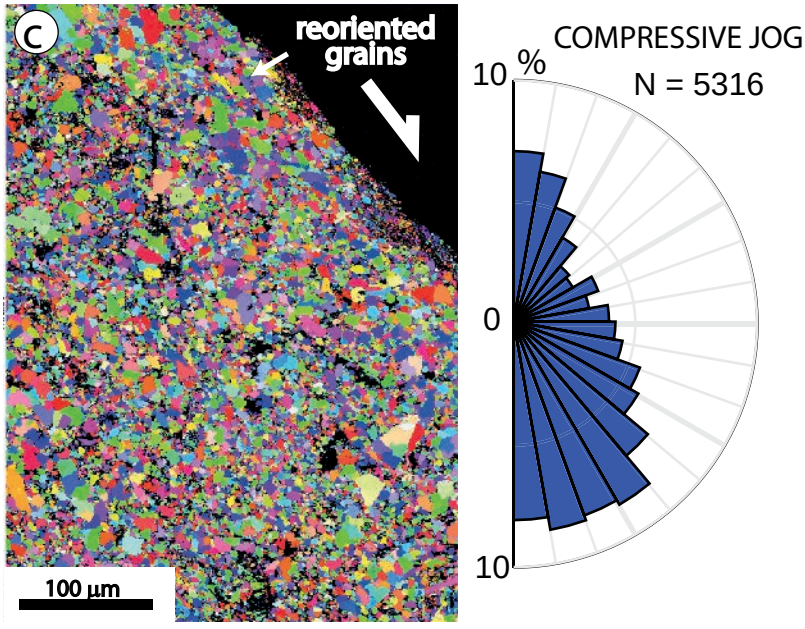
c
reorientated
grains
100 µm
COMPRESSIVE JOG
N = 5316
%
10
0
10

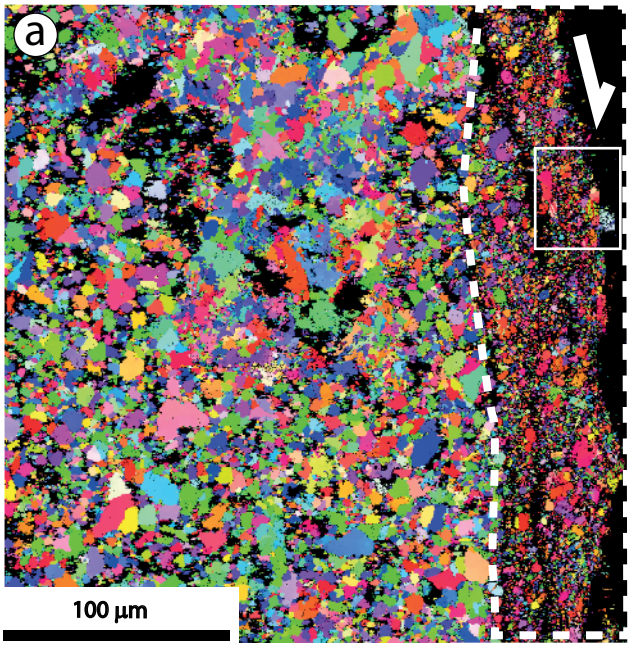
a
100 µm

Fig. 14a

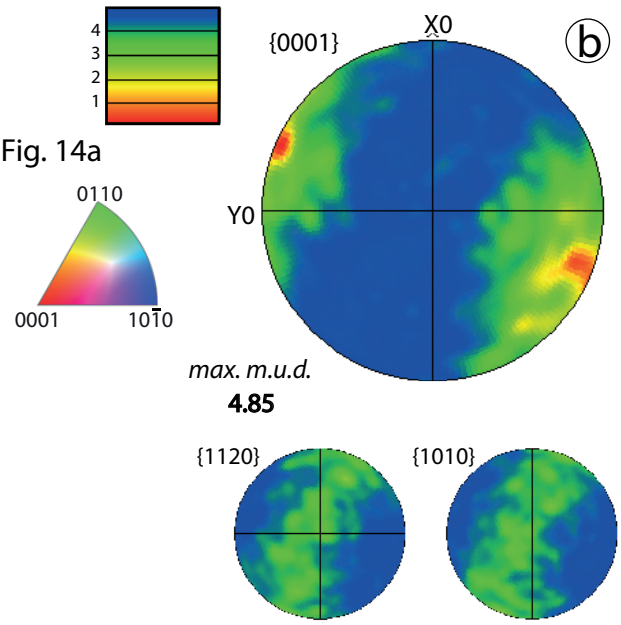
4
3
2
1
0110
0001
10$\bar{1}$0
{0001}
X0
Y0
b
max. m.u.d.
4.85
{1120}
{1010}

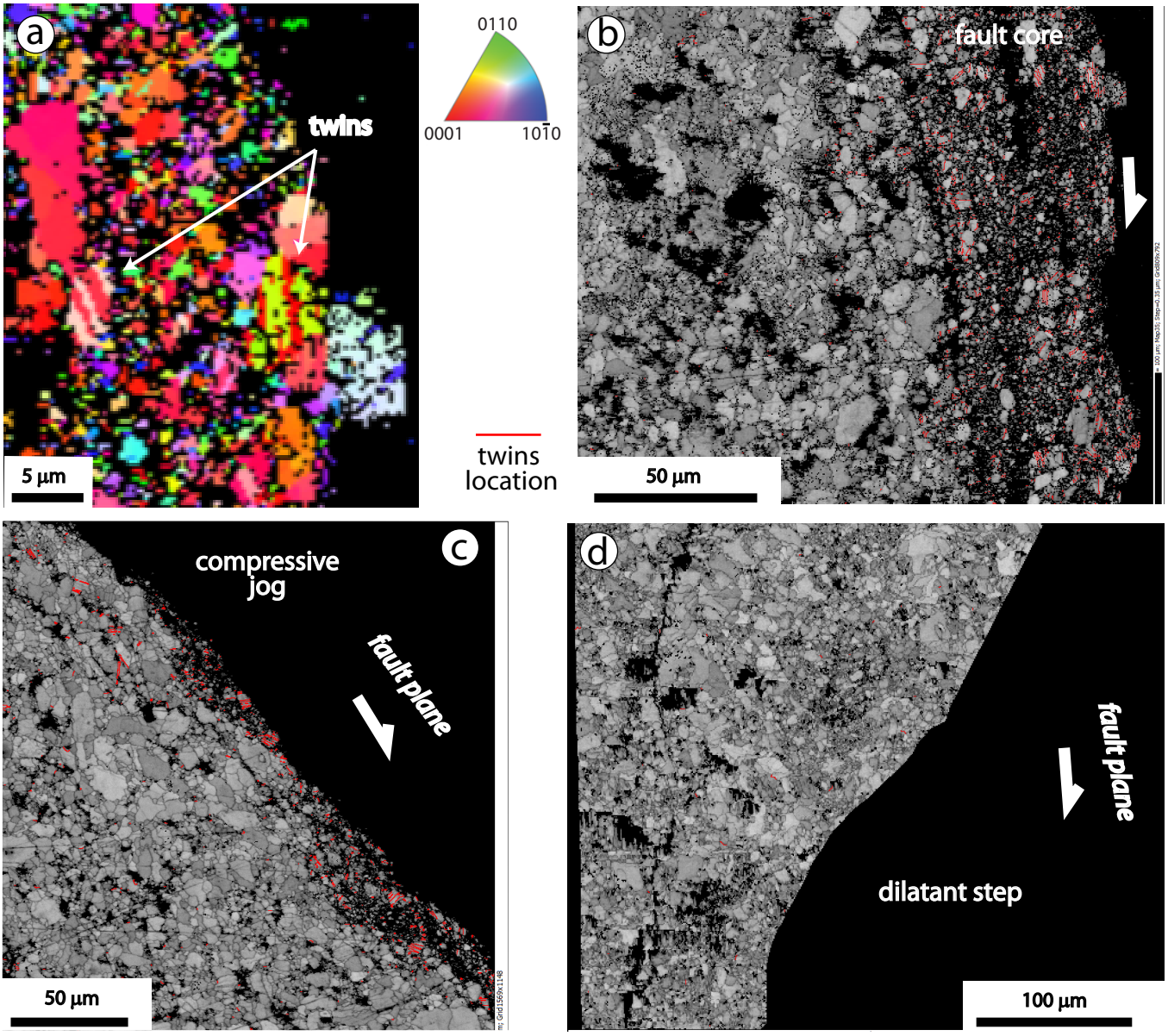
a
twins
5 µm
0110
0001
1010
twins
location
b
fault core
50 µm
c
compressive
jog
fault plane
50 µm
d
fault plane
dilatant step
100 µm

a

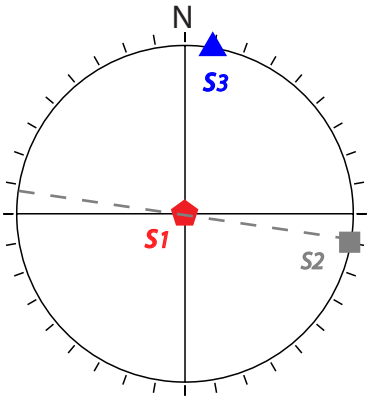

r0 = 0.00
S1 = 274°/90°
S2 = 99°/0°
S3 = 9°/0°

b

Stress tensor	Ntotal	Pinv (%)	$\Delta\lambda_{av}$ (°)	N_{exp15}	$N0_{exp15}$	InvQual
	264	99	9.6	216	25.7	2

c

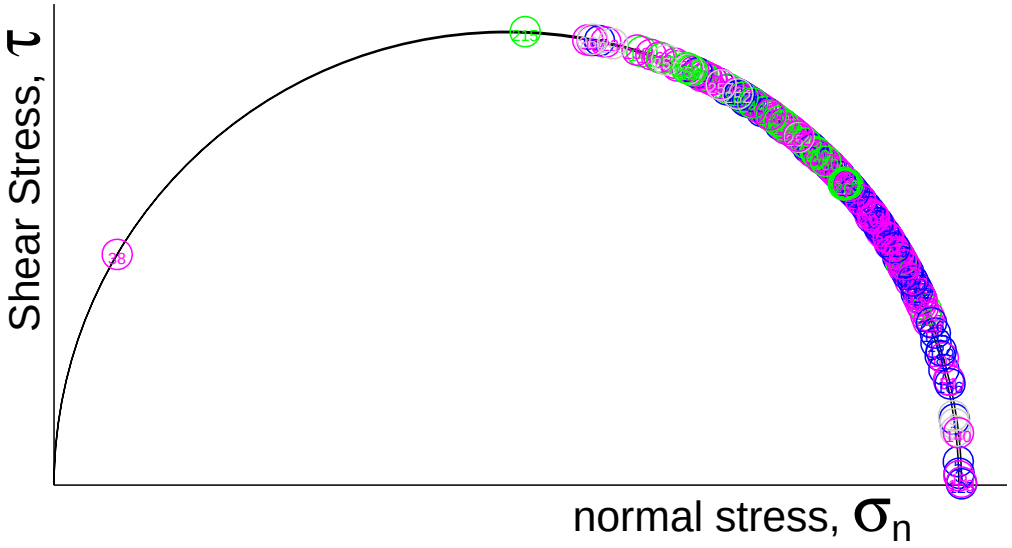

Angle misfit range

- 0° << 5°
- 5° < < 15°
- 15° < < 30°
- 30° < < 180°


a
S0
50 cm
multi-beds
normal fault

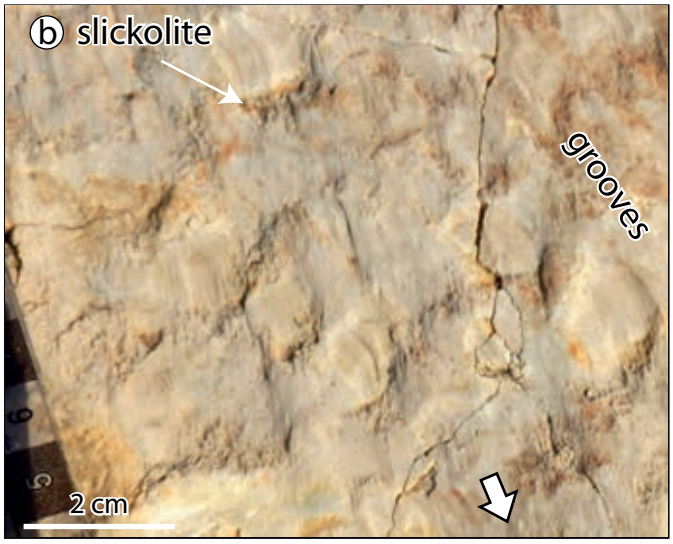
b slickolite
grooves
2 cm

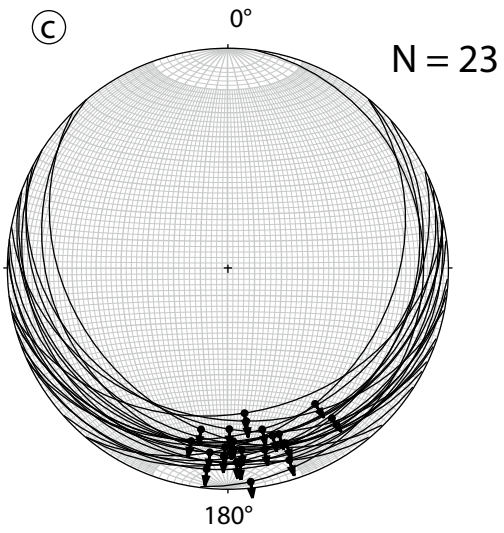
c
0°
N = 23
180°

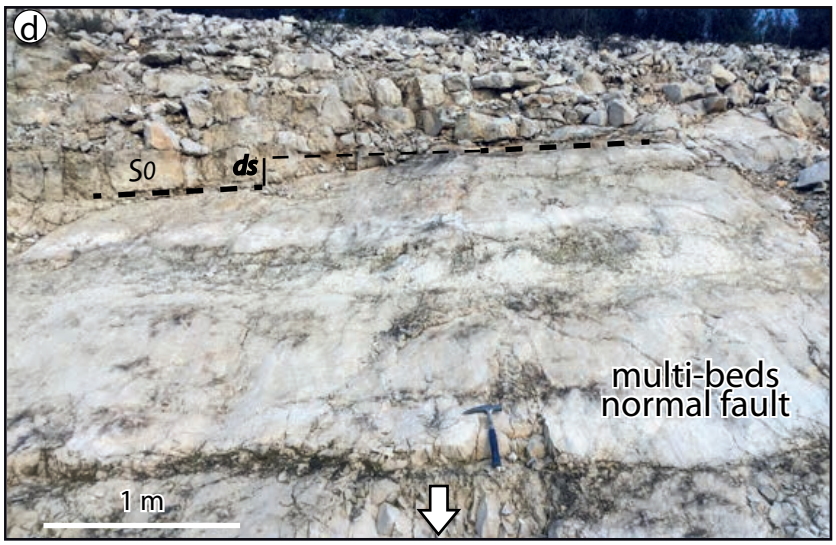
d
S0
ds
multi-beds
normal fault
1 m

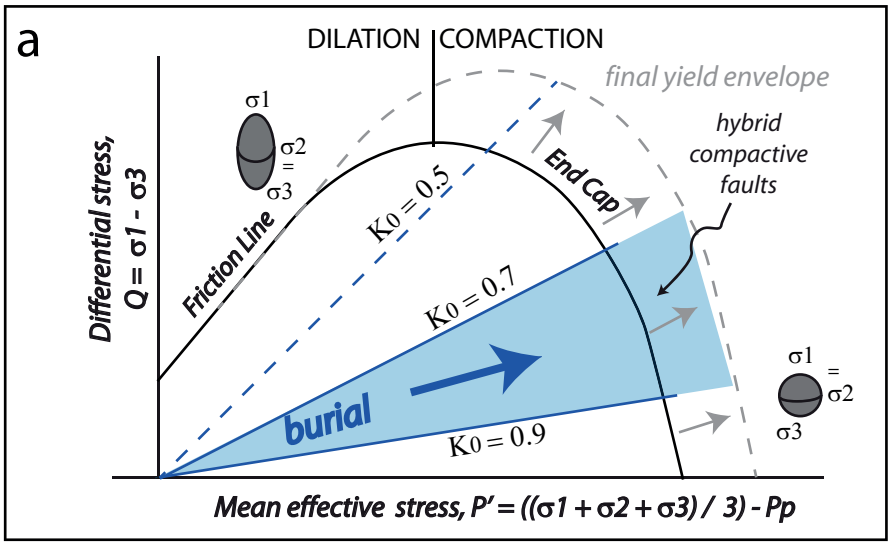
a
DILATION
COMPACTION
final yield envelope
hybrid compactive faults
End Cap
Friction Line
Differential stress, Q = σ1 - σ3
σ1
σ2 = σ3
K0 = 0.5
K0 = 0.7
K0 = 0.9
burial
σ1 = σ2
σ3
Mean effective stress, P' = ((σ1 + σ2 + σ3) / 3) - Pp

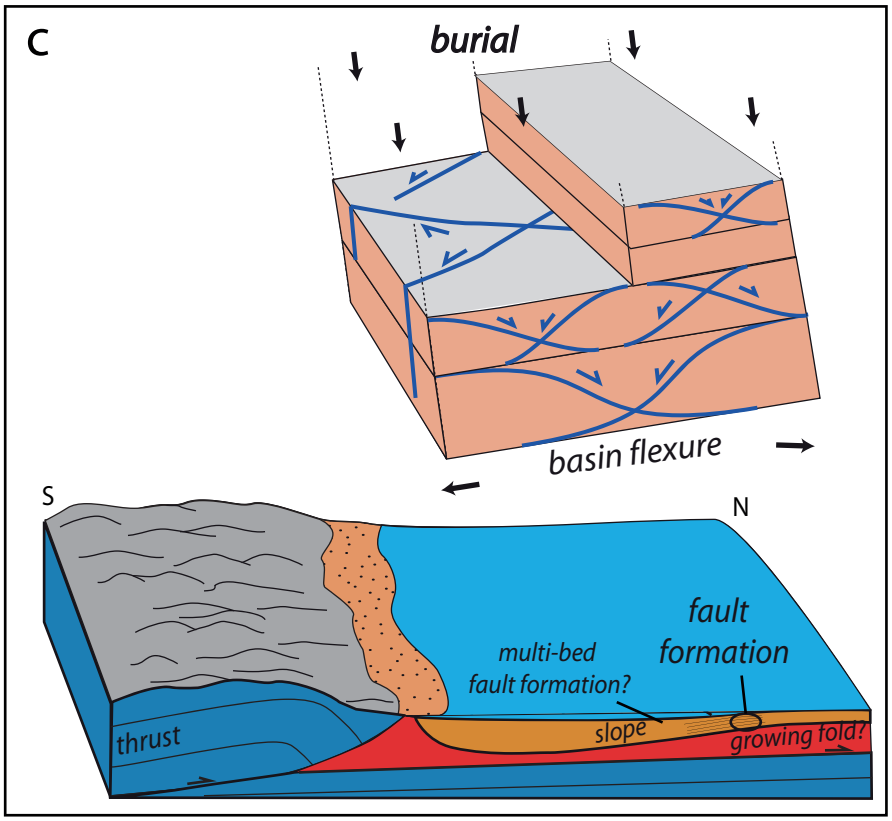
c
burial
basin flexure
S
N
fault formation
multi-bed fault formation?
slope
growing fold?
thrust

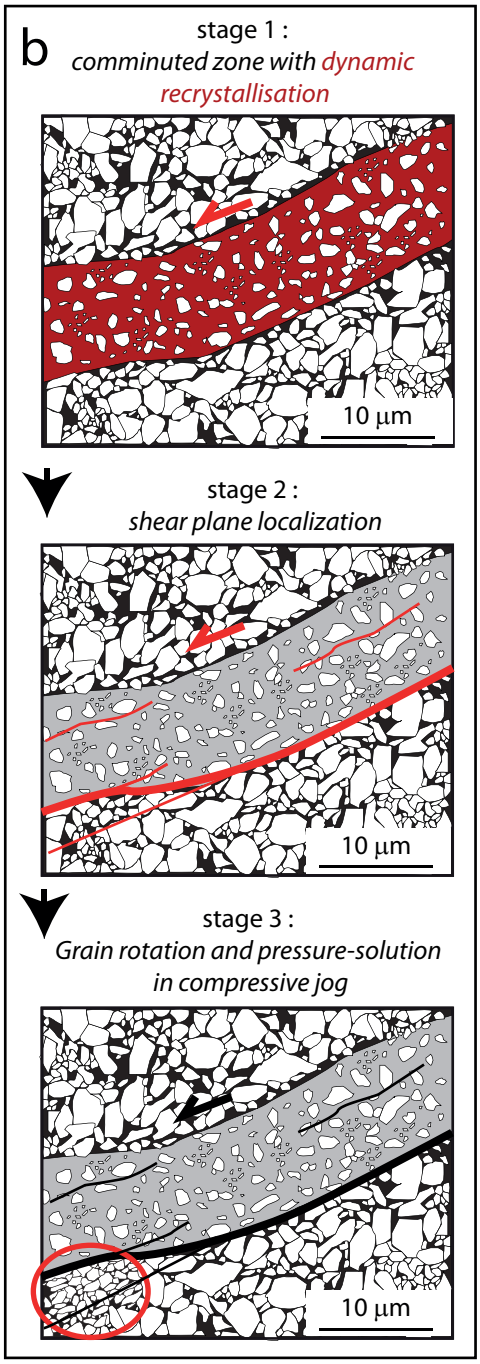
b
stage 1 :
comminuted zone with dynamic recrystallisation
10 µm
stage 2 :
shear plane localization
10 µm
stage 3 :
Grain rotation and pressure-solution in compressive jog
10 µm